Supporting information for

3D Porous Graphitic Nanocarbon for Enhancing Durability of Pt Catalysts: Balance between graphitization and hierarchical porosity

Zhi Qiao[a,1], Sooyeon Hwang[b,1], Xing Li[b,h,1], Chenyu Wang[c,1], Widitha Samarakoon[d], Stavros Karakalos[e], Dongguo Li[c], Mengjie Chen[a], Yanghua He[a], Maoyu Wang[d], Zhenyu Liu[g], Guofeng Wang[g], Hua Zhou[f], Zhenxing Feng *[d], Dong Su*[b], Jacob S. Spendelow*[c] and Gang Wu*[a]

[a], Department of Chemical and Biological Engineering, University at Buffalo, The State University of New York, Buffalo, New York 14260, United States

[b], Center for Functional Nanomaterials, Brookhaven National Laboratory, Upton, New York 11973, United States

[c], Materials Physics and Applications Division, Los Alamos National Laboratory, Los Alamos, New Mexico 87545, United States

[d], School of Chemical, Biological, and Environmental Engineering, Oregon State University, Corvallis, Oregon 97333, United States

[e], Department of Chemical Engineering, University of South Carolina, Columbia, South Carolina 29208, United States

f X-ray Science Division, Argonne National Laboratory, Argonne, Illinois 60439, United States

[g], Department of Mechanical Engineering and Materials Science, University of Pittsburgh, Pittsburgh, PA 15261, United States

[h], Department of Physics and Engineering, Key Laboratory of Material Physics, Zhengzhou University, Zhengzhou, 450052, China

* Corresponding authors: zhenxing.feng@oregonstate.edu (Z. Feng); dsu@bnl.gov (D. Su); spendelow@lanl.gov (J.S. Spendelow); and gangwu@buffalo.edu (G. Wu)

[1] These authors contributed equally.

Experimental details

Figures S1 to S34

Tables S1 to S5

1. Experimental details

1.1 Synthesis of Mn-hydrogel derived porous graphitic carbons

To prepare Mn-PANI hydrogel-derived PGC, we first dissolved 1.32 g (14.16 mmol) aniline and 1.62 g (7.08 mmol) ammonium persulfate (APS) in separate 2.0 M hydrochloric acid (HCl) solutions (6 mL each). These two solutions were denoted as solution A (aniline solution) and solution B (APS solution). Subsequently, 2.8 g (14.16 mmol) manganese chloride tetrahydrate was dissolved into solution A. Then, solution B was gradually added into solution A, and shaken gently in a vial for 30 seconds. The resulting gel-like mixture was aged at room temperature for 24 h. Freeze-drying was used to remove solvent while retaining the porous structure of the PANI hydrogel composite. The resulting solid powder was processed by thorough grinding followed by a heat treatment at 900, 1000 or 1100°C for 1 h under nitrogen (N_2) flow with a ramp rate of 3°C/min. The pyrolyzed solid powder was leached with 0.5 M H_2SO_4 at 80°C for 5 h and then dried at 60°C in a vacuum oven for 12 h. A second heat treatment was then carried out at 900°C for 3 h under N_2 flow with a ramp rate of $3^{\circ C}$/min. The obtained sample heated at 1100°C (the first heat treatment) is denoted as Mn-PANI-PGC. For Mn-PANI-PPy-PGC, 0.47 g (7.08 mmol) pyrrole was added together with aniline in solution A, and other steps and procedures remained the same.

1.2 Method to deposit Pt nanoparticles.

Pt nanoparticle deposition onto the Mn-hydrogel-derived PGC supports was performed through an ethylene glycol (EG) reduction method with a controlled Pt mass loading of 20 wt%. The carbon support powder was dispersed in EG by sonication for 1 hour to form a homogeneous complex suspension. Then, a given amount of hexachloroplatinic acid solution (10 mg/mL) was added into EG solution under stirring for 20 minutes with N_2 bubbling. The suspension was refluxed for 4 hours at 130°C under continuous stirring. The catalysts were washed with Millipore water until no Cl^- could be detected by $AgNO_3$ solution and dried at 60°C in a vacuum oven for 12 hours. The as-prepared samples were subsequently heat-treated in N_2 at 800°C for 30 mins. The final catalysts were identified as Pt/Mn-PANI-PGC or Pt/Mn-PANI-PPy-PGC when Mn-PANI and Mn-PANI-PPy hydrogel were used for carbon preparation, respectively.

1.3 Physical characterization

Raman spectra were collected on a Renishaw Raman system at 514 nm laser source to analyze carbon structures. Excitation power was held constant at ∼150 μW for all samples, which were prepared as powders on a glass surface. The excitation laser was focused through a 100× microscope objective for a total interrogation spot size of ∼ 1 micron diameter. Scattered light was collected in backscatter configuration into an optical fiber and then dispersed through the Renishaw spectrometer and projected onto a CCD camera. Brunauer-Emmett-Teller (BET) surface area and porosity were measured by using N_2 adsorption/desorption at 77 K on a Micromeritics TriStar II. Scanning electron microscopy (SEM) images were obtained on a Hitachi SU 70 microscope at a working voltage of 5 kV. Bright field and high-resolution transmission electron microscopy (HRTEM) images, and scanning TEM-energy dispersive spectroscopy (STEM-EDS) elemental maps were obtained with a Talos F200X (Thermo Fisher Scientific) at an accelerating voltage of 200 kV.

For in-situ analysis, samples were firstly dispersed in methanol and the suspension was deposited directly onto a thermal chip (DENS Solutions). The temperature was controlled with a MEMS heating stage from DENS Solutions. The in-situ electron microscopy was performed on an aberration-corrected transmission electron microscopy (FEI Titan 80/300), operating at 300 kV. The beam was blanked during the in-situ heating processes and the samples were only exposed to the beam during date setup and acquisition processes. The element mapping was conducted on a high-resolution analytical scanning/transmission electron microscope (S/TEM, FEI Talos F200X) operating at 200 keV. The elemental mappings were acquired with a four-quadrant 0.9-sr energy dispersive X-ray spectrometer (Super EDS).

X-ray diffraction (XRD) was conducted by using a Rigaku Ultima IV diffractometer with Cu K-α X-rays. X-ray photoelectron spectroscopy (XPS) was performed with a Kratos AXIS Ultra DLD XPS equipped with a hemispherical energy analyzer and a monochromatic Al Kα source operated at 15 keV and 150 W and pass energy was fixed at 40 eV for the high-resolution scans. Samples were prepared as pressed powder supported on a metal bar for the measurements. The FWHM of the major XPS peaks ranged from 0.3 eV to 1.7 eV for the relevant elements. All the instrument parameters were constant including FWHMs, peak shapes, instrument design factors, chemical shifts, experimental settings and sample factors. The binding energy of Au was used as the reference. Pt particle size distributions were measured by TEM images of more than 200 particles for different catalysts. Pt L_3-edge X-ray absorption spectroscopy (XAS) including X-ray absorption near edge structure (XANES) and extended X-ray absorption fine structure (EXAFS) experiments were carried out at beamline 20-BM at the Advanced Photon Source, Argonne National Laboratory. The EXAFS data were collected in transmission mode and the energy scale was using a Pt foil. Data analysis was performed using the Athena and Artemis software packages.

1.4. Electrochemical measurements

All electrochemical measurements were performed on a CHI Electrochemical Station (Model 760b) equipped with high-speed rotators from Pine Instruments. A rotating ring disk electrode (RRDE) from Pine Research Instrumentation (model: AFE7R9GCPT, USA) was used as the working electrode, containing glassy carbon disk and platinum ring: disk OD = 5.61 mm; ring OD = 7.92 mm; ID = 6.25 mm. An $Hg/HgSO_4$ reference electrode and a graphite rod counter electrode with a diameter of 0.250 inches and a length of 12 inches were used to complete the cell. To prepare the working electrode, 10 mg catalyst was dispersed ultrasonically in a 1.0 mL mixture of isopropanol and Nafion (5 wt.%) solution to form an ink. Then the ink was drop-casted on the disk electrode with a designed loading of 20 $\mu g_{Pt}/cm^2$ or 60 $\mu g_{Pt}/cm^2$ and dried at room temperature to yield a thin-film electrode. All the cyclic voltammetry (CV) and ORR polarization curves were recorded in 0.1 M $HClO_4$ and the ORR activity was measured in 0.1 M $HClO_4$ saturated with O_2 at 900 rpm or 1600 rpm using steady-state polarization plots by holding each potential for 30s with potential step of 30 mV. The accelerated stress tests (ASTs) were applied to evaluate catalyst stability by cycling the potentials in both low (0.6−1.0 V, 50 mV/s, 25°C) and high (1.0−1.5 V, 500 mV/s, 60°C) potential ranges in 0.1 M $HClO_4$ saturated with N_2 by using RDE. All reference potentials have been converted to reversible hydrogen electrode (RHE). As comparison, three kinds of Pt/C catalyst from TKK were studied regarding to activity and durability, including TEC10V20E, TEC10EA20E and TEC10E20E.

1.5 Fuel Cell Fabrication and Testing

Catalysts were incorporated into MEAs by spraying of a water/n-propanol based ink onto a 5 cm2 area of a Nafion 211 membrane. Each electrode was prepared with Pt loading of 0.1 $mgPt/cm^2$, and 29BC gas diffusion layers (SGL Carbon) were used on both anode and cathode. H_2-air fuel cell testing was carried out in a single cell using a commercial fuel cell test system (Fuel Cell Technologies Inc.). The MEA was sandwiched between two graphite plates with straight parallel flow channels machined in them. The cell was operated at 80°C, with 150 kPa_{abs} H_2/air or H_2/O_2, and a gas flow rate of 500/2000 sccm for anode/cathode, respectively. Catalyst mass activity was measured via the DOE/FCTT protocol (potential step from 0.6 V to 0.9 V and 15 min hold, current averaged during last 1 min) in 150 kPa_{abs} H_2/O_2 (80°C, 100% RH, 500/2000 sccm) with correction for measured H_2 crossover. The ECSA was obtained by calculating H adsorption charge in CV curves between 0.1-0.4 V (0.45-0.55 V background subtracted) at 30-35°C with 500 sccm H_2 on the anode and stagnant N_2 on the cathode, assuming a value 210 $\mu C/cm^2$ for the adsorption of a H monolayer on Pt. The low-potential catalyst AST was conducted by using trapezoidal wave cycling from 0.6 V to 0.95 V with 0.5 s rise time and 2.5 s hold time, while the high-potential support AST was conducted using triangle wave cycling from 1.0 to 1.5 V (150 kPa_{abs} H_2/N_2, 80°C, 100%RH, 200/200 sccm H_2/N_2). Carbon corrosion rates were determined through measurement of CO_2 concentration in the cathode effluent gas by non-dispersive infrared spectroscopy.

1.6. Computational methods

The spin-polarized density functional theory (DFT) calculations were performed using plane wave basis and Projector Augmented Wave (PAW) formalism, as implemented in the Vienna Ab-initio Simulation Package (VASP)[1-4]. The generalized-gradient approximation (GGA) in the form of Perdew-Burke-Ernzerhof (PBE) functionals were employed to evaluate the exchange-correlation energy[5]. The kinetic energy cutoff of 500 eV was used for plane wave expansion and the total energy was converged to 10^{-6} eV. The structures were optimized until the force acting on each atom was below 0.01 eV/Å. The carbon support was modeled using a hexagonal 7×7 supercell of graphene layer containing 98 carbon atoms, with the in-plane lattice constant equal to the optimized value of 2.468 Å. The Brillouin zone was sampled using a Gamma centered k-point mesh of 2×2×1. A vacuum layer of 20 Å was added above the graphene layer to avoid the interaction between periodic images. One N atom was doped into the modeled graphene layer, giving a nominal doping concentration of about 1 at%. Single Pt atom and Pt_{13} cluster were allowed to adsorb on the undoped and N-doped graphene (N-C) layer. The binding energy E_b is defined as

$$E_b(Pt/C) = E_{Pt/C} - E_{Pt} - E_C$$

where $E_{Pt/C}$ is the total energy of the Pt/graphene system, E_{Pt} is the total energy of Pt atom or Pt cluster, and E_C is the total energy of the graphene layer. The metric we adopted to evaluate the relative stability of Pt adsorption is the binding energy difference between the defective graphene $E_b(Pt/N-C)$ and pristine graphene $E_b(Pt/C)$, which was calculated as follows

$$\begin{aligned} \Delta E_b &= E_b(Pt/N-C) - E_b(Pt/C) \\ &= (E_{Pt/N-C} - E_{N-C}) - (E_{Pt/C} - E_C) \end{aligned}$$

Additional physical characterization and electrochemical measurements

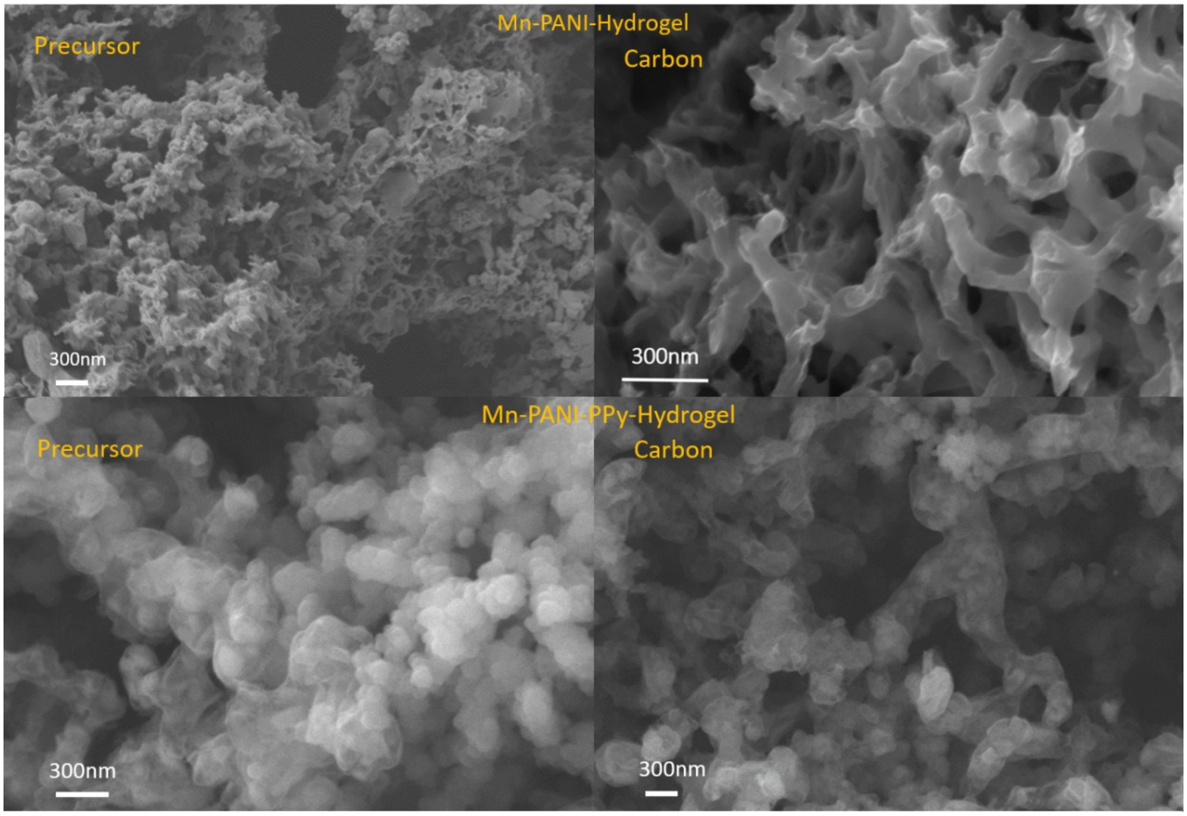

Figure S1. SEM images for two kinds of PGCs and their precursors.

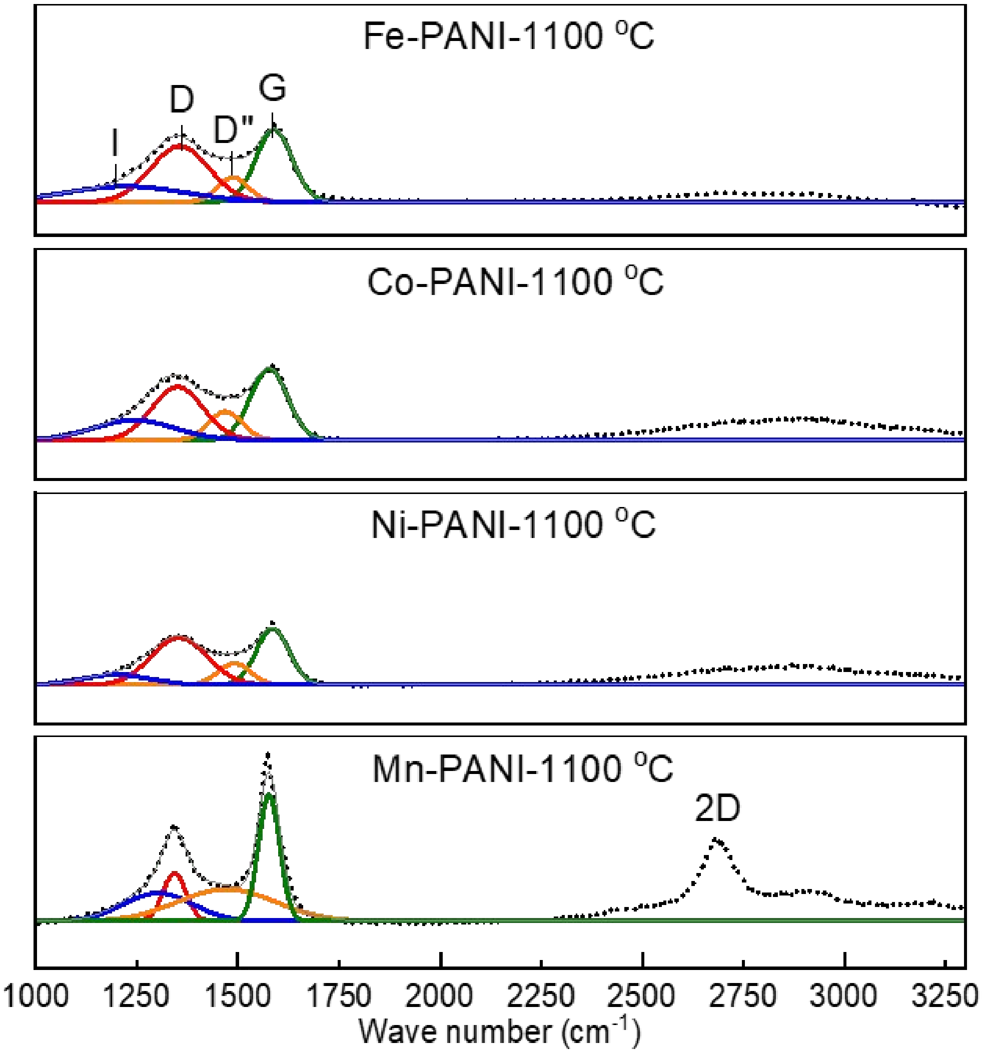

Figure S2. Raman spectra for different hydrogel based carbons derived from different metals with identical method.

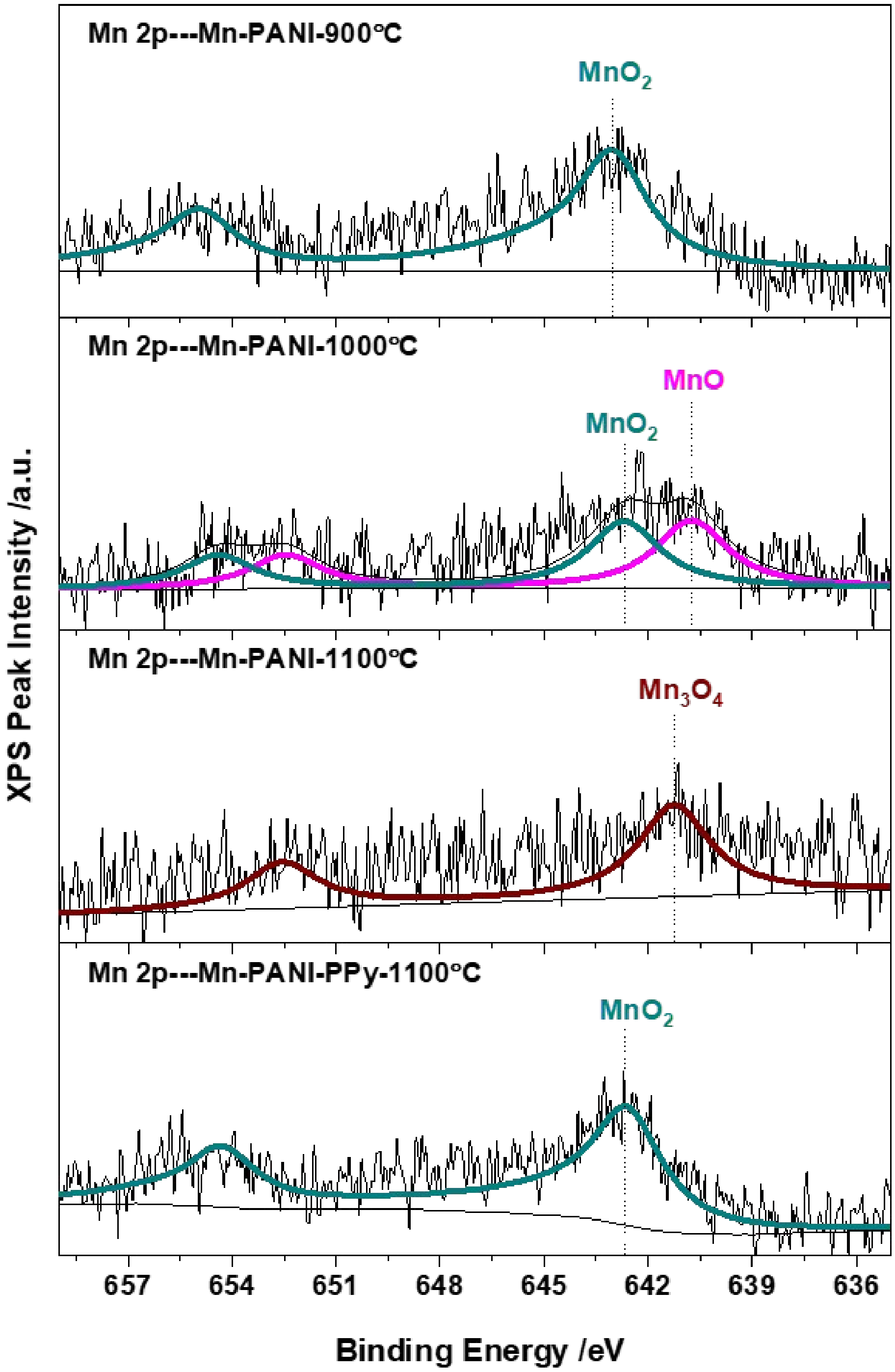

Figure S3. High-resolution XPS Mn 2p spectra of different PGCs derived from different temperature.

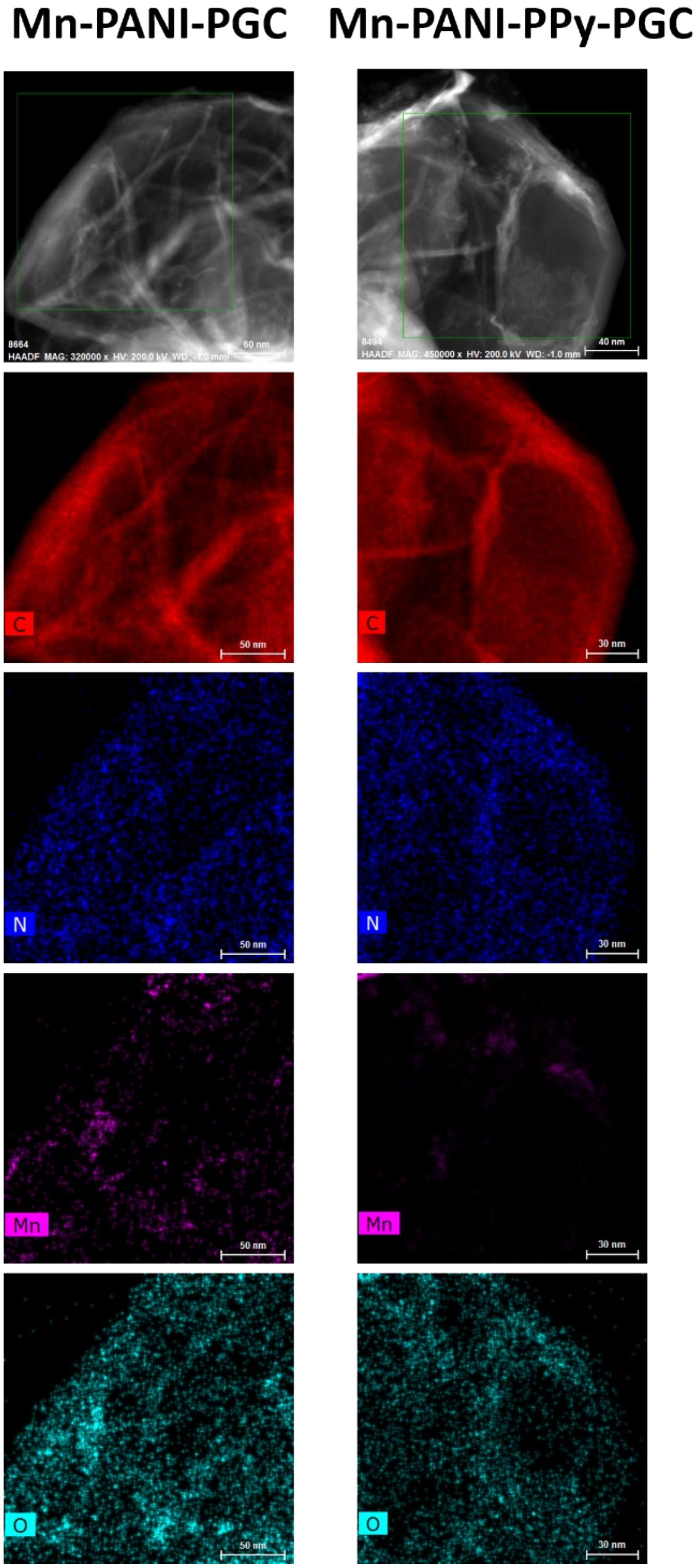

Figure S4. More STEM-EDS mapping images for two kinds of PGCs.

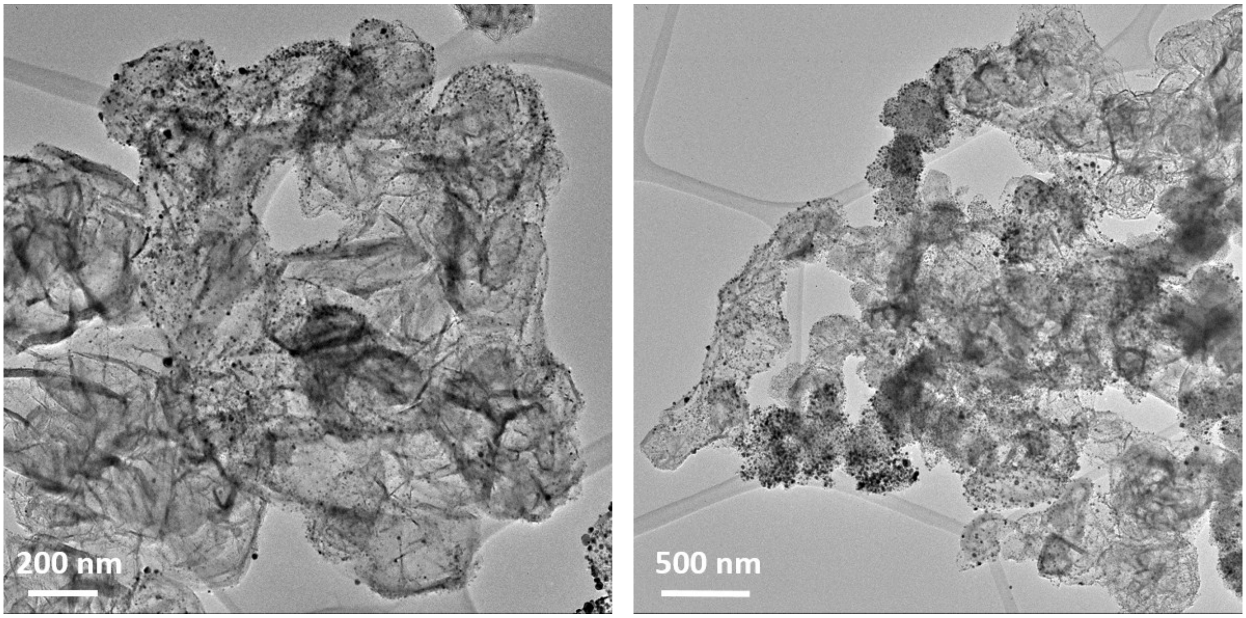

Figure S5. TEM images of Pt/Mn-PANI-PPy-PGC.

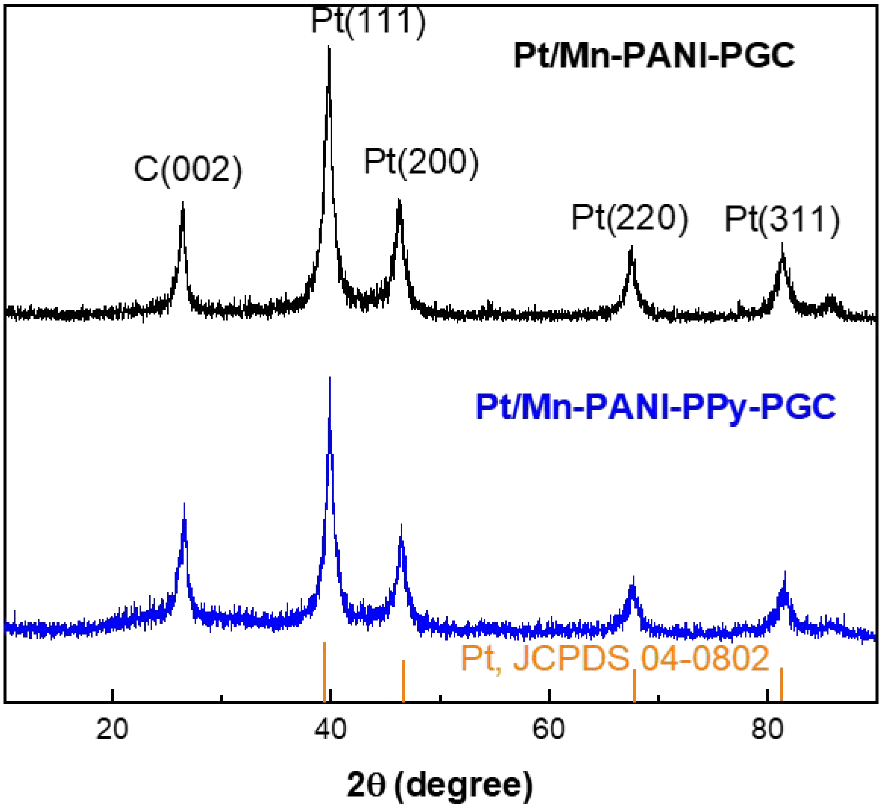

Figure S6. XRD spectra of two kinds of Pt catalysts supported on Mn-PANI-PGC and Mn-PANI-PPy-PGC respectively

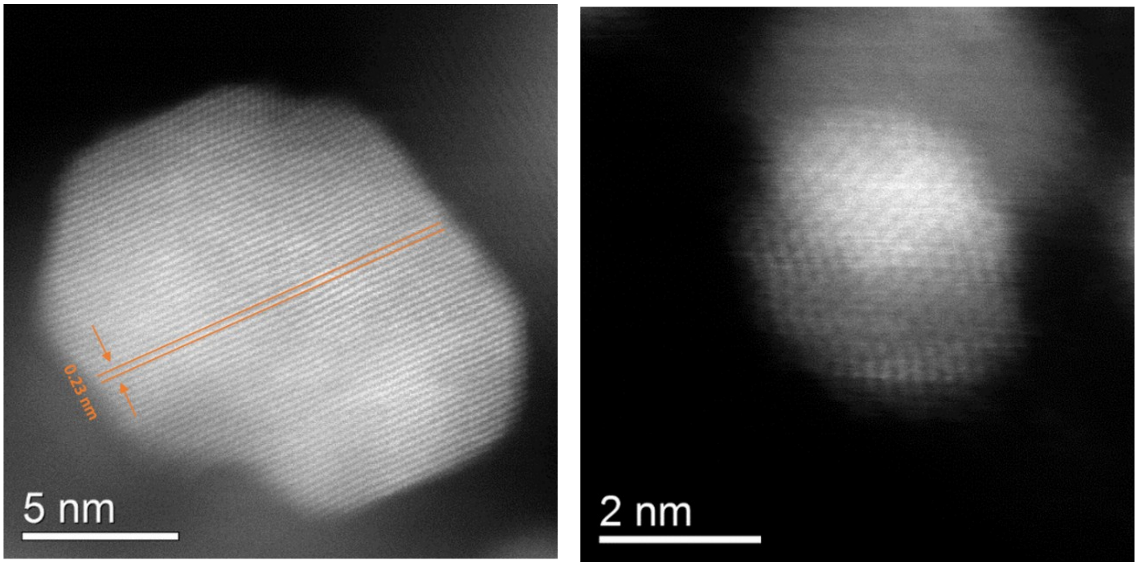

Figure S7. STEM images of Pt/Mn-PANI-PPy-PGC.

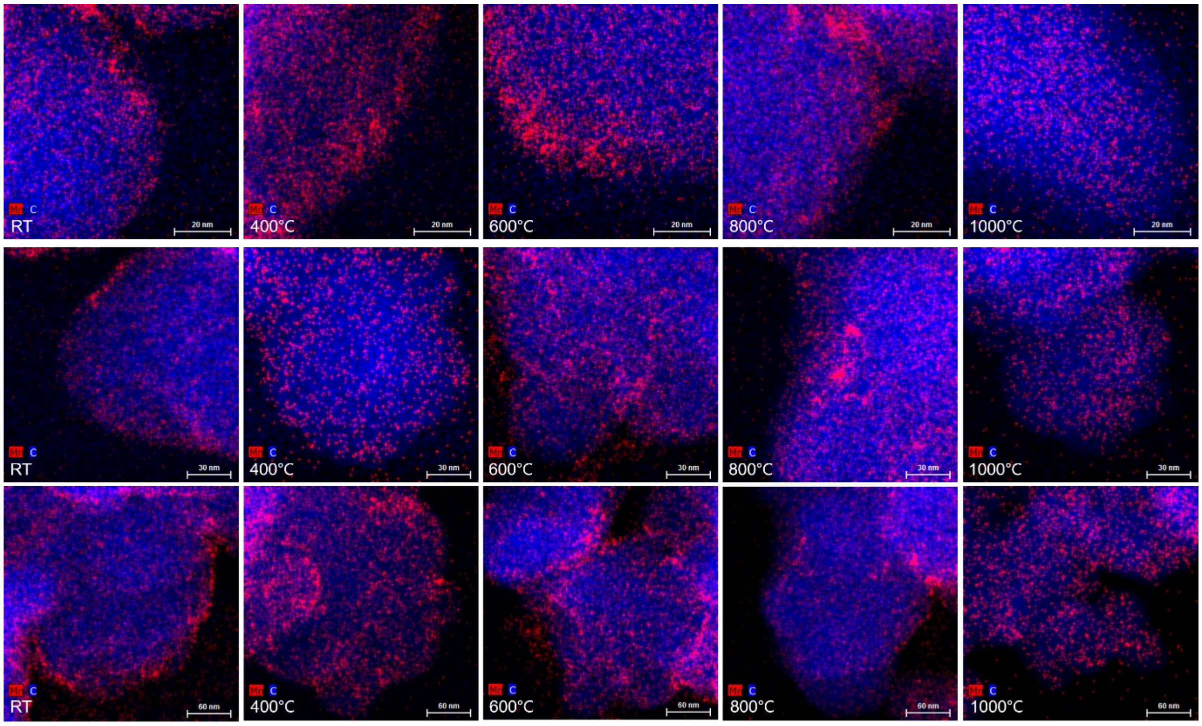

Figure S8. In-situ STEM-EDS mapping images of Mn-PANI-PPy precursor at different temperatures.

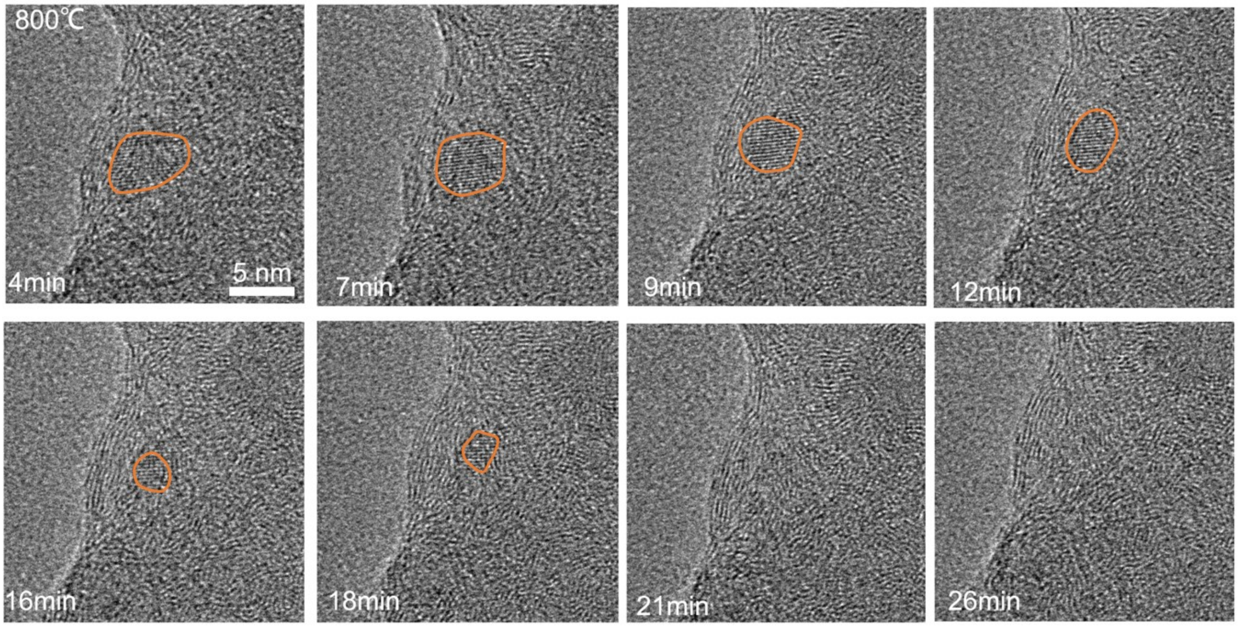

Figure S9. In-situ HRTEM images of Mn-PANI-PPy precursor at 800°C (Mn species circled by orange curves).

Table S1. XPS summary for different PGCs derived from different temperature.

	S (at%)	C (at%)	N (at%)	O (at%)	Mn (at%)
Carbon-Mn-PANI-900^{o}C	0.3	95.1	2.0	2.4	0.2
Carbon-Mn-PANI-1000^{o}C	0.2	96.3	1.0	2.2	0.2
Mn-PANI-PGC-1100^{o}C	0.1	97.8	0.7	1.1	0.3
Mn-PANI-PPy-PGC-1100^{o}C	0.1	97.8	0.7	1.0	0.4

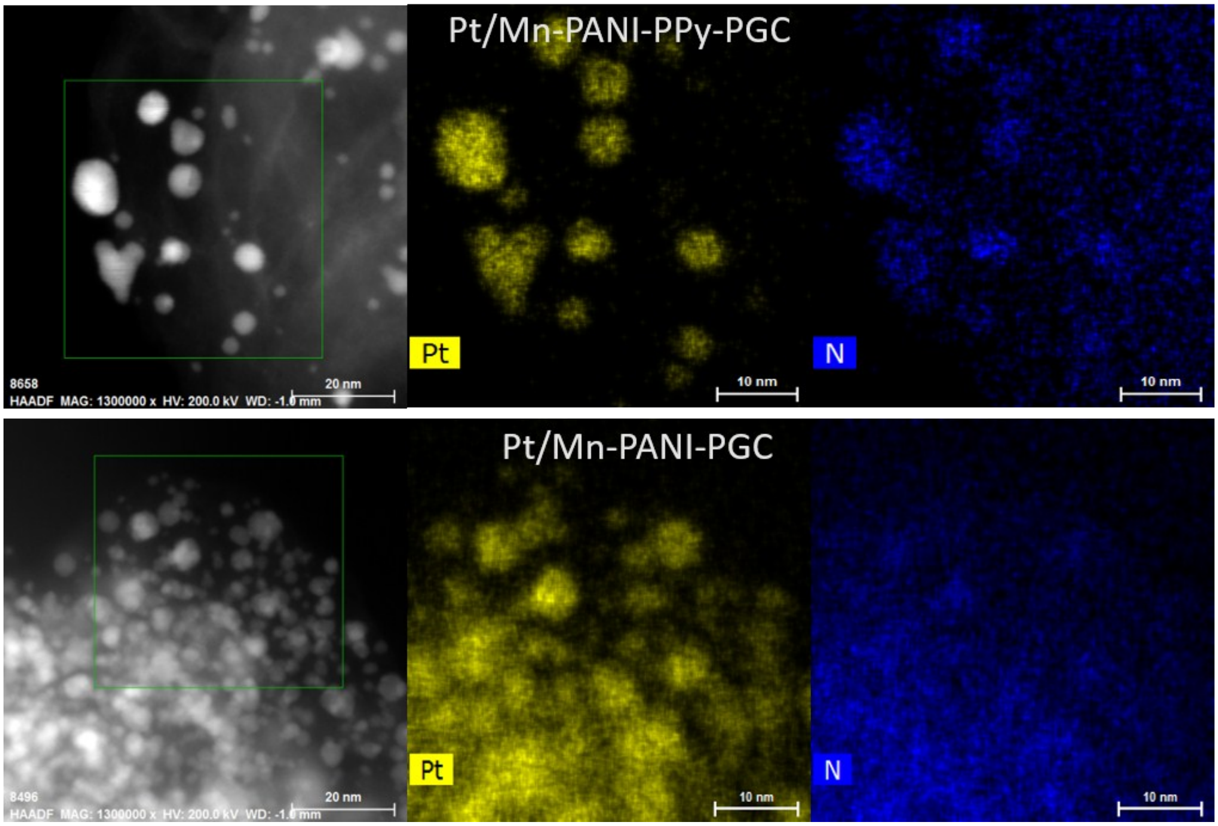

Figure S10. STEM-EDS elemental mapping of **(Above)** Pt/Mn-PANI-PPy-PGC and **(Below)** Pt/Mn-PANI-PGC. (Both catalysts were obtained after post heat treatments.)

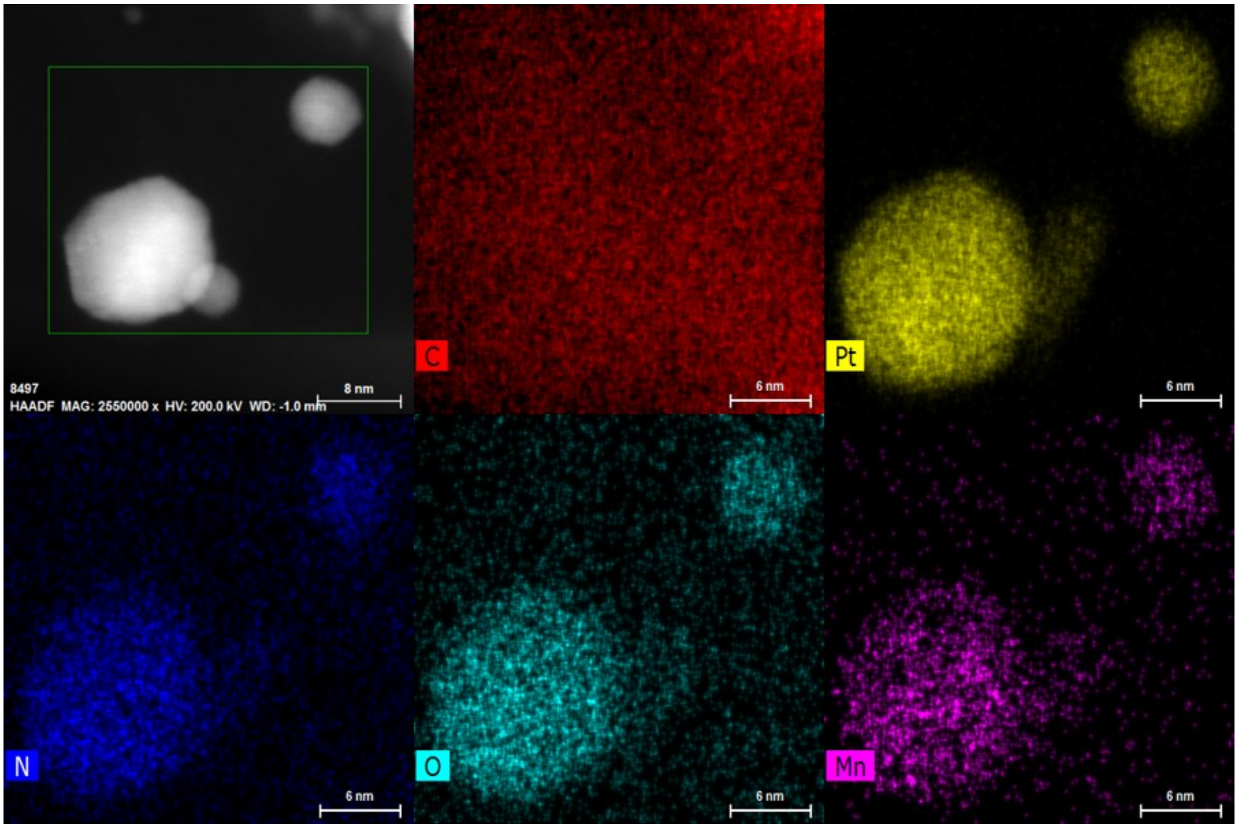

Figure S11. STEM-EDS elemental mapping of Pt/Mn-PANI-PPy-PGC.

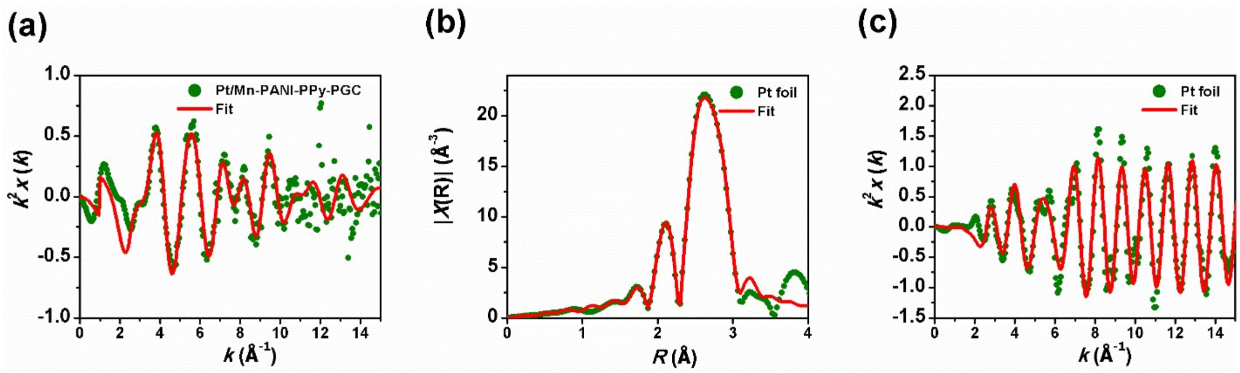

Figure S12 (a) The EXAFS fitting result for Pt/Mn-PANI-PPy-PGC using Pt-Pt and Pt-N scattering paths in *k* space. **(b)** The EXAFS fitting result for Pt foil in *R* space. (c) The EXAFS fitting result for Pt foil in *k* space.

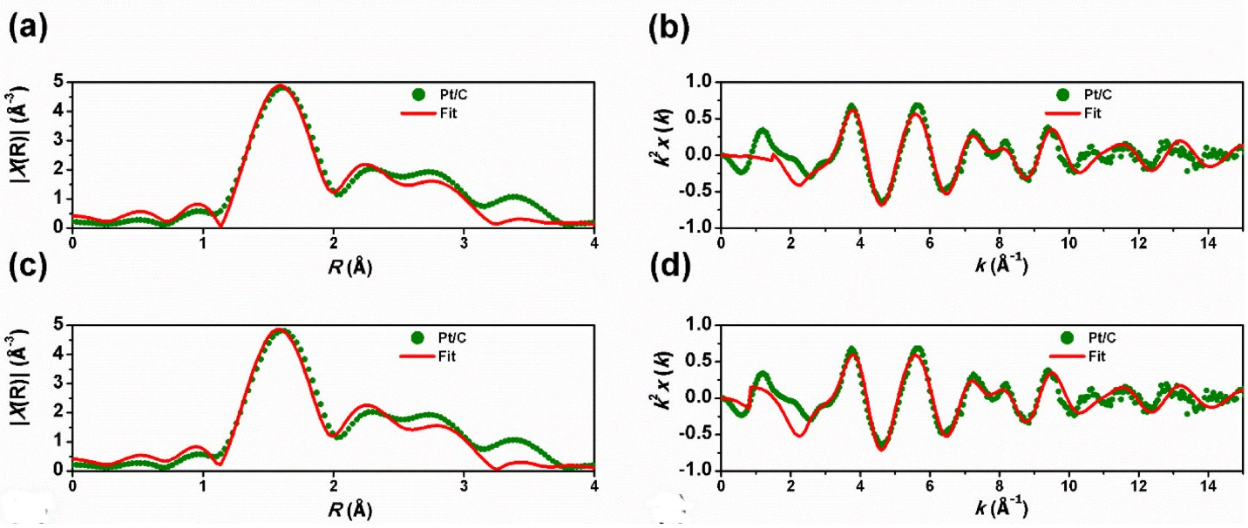

Figure S13. The EXAFS fitting results for Pt/C using different combinations of scattering paths **(a)** The EXAFS fitting results using Pt-Pt and Pt-O scattering paths in *R* space and, **(b)** *k* space **(c)** The EXAFS fitting results using Pt-Pt and Pt-C scattering paths in *R* space and, **(d)** *k* space.

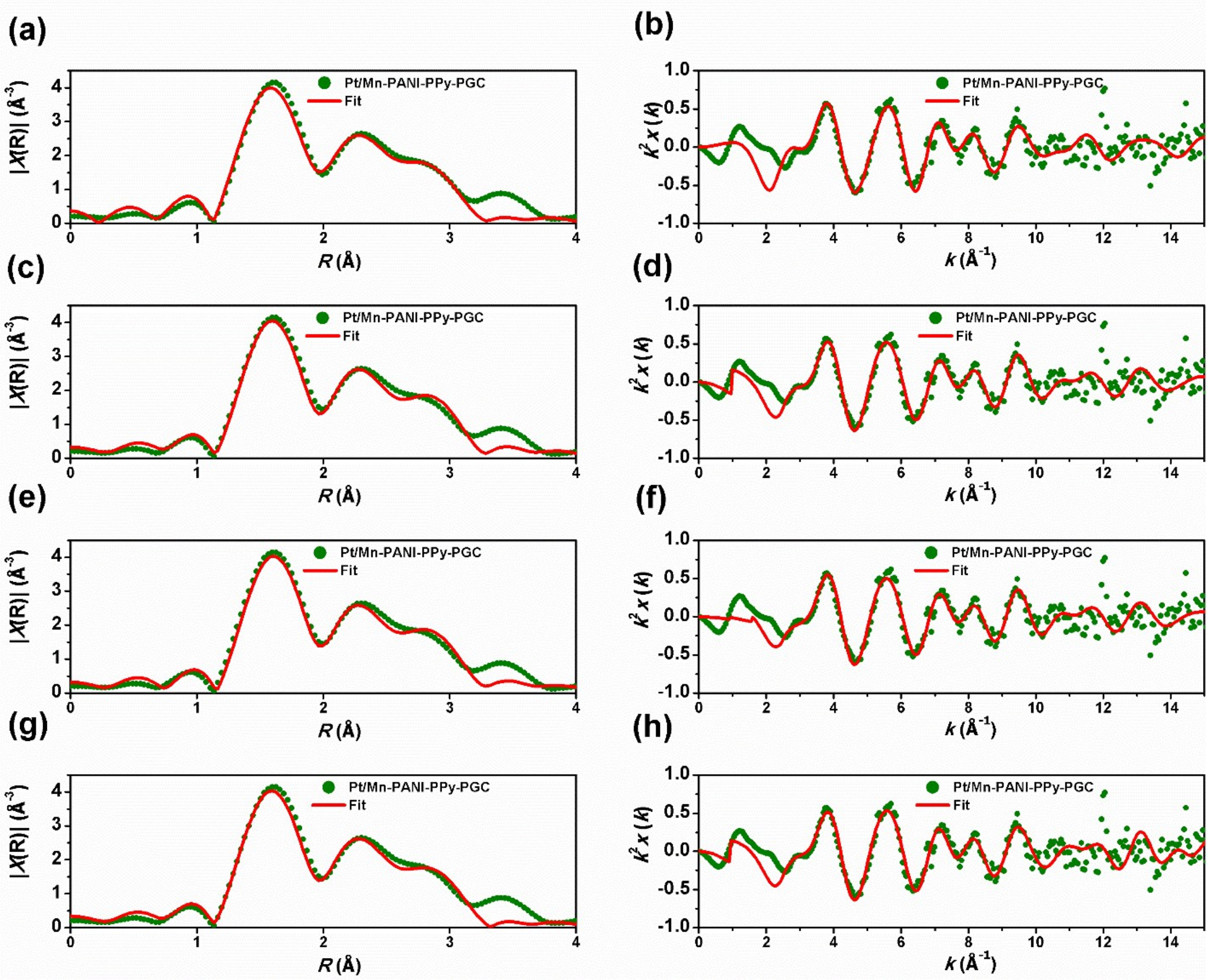

Figure S14. The EXAFS fitting results for Pt/Mn-PANI-PPy-PGC using different combinations of scattering paths **(a)** The EXAFS fitting results using Pt-Pt and Pt-C scattering paths in *R* space and, **(b)** *k* space **(c)** The EXAFS fitting results using Pt-Pt, Pt-C and Pt-N scattering paths in *R* space and, **(d)** *k* space **(e)** The EXAFS fitting results using Pt-Pt and Pt-O scattering paths in *R* space and, **(f)** *k* space **(g)** The EXAFS fitting results using Pt-Pt, Pt-N and Pt-O scattering paths in *R* space and, **(h)** *k* space.

Table S2. EXAFS fitting results for Pt/C using different combinations of scattering paths. N, coordination number, R, the distance between the absorber and scatterer atoms, σ^2, Debye-Waller factor to account for thermal and structural disorders, ΔE_0, inner potential correction. Fitting range, $2.5 \leq k(\text{Å}^{-1}) \leq 10$ and $1 \leq R(\text{Å}) \leq 3.2$; Fixed N according to the crystal structure. Error bounds indicated in parenthesis are full errors for N and last digit errors for other parameters.

Paths		Pt-Pt				Pt-O				Pt-C			
Fit	χ^2	N	R (Å)	σ^2 (Å^2)	ΔE_0 (eV)	N	R (Å)	σ^2 (Å^2)	ΔE_0 (eV)	N	R (Å)	σ^2 (Å^2)	ΔE_0 (eV)
1	986	6.6(2.0)	2.70(3)	0.013(6)	1.5(6)	1.8(0.3)	3.02(2)	0.001(1)	8.5(1)	-	-	-	-
2	1544	23.3(7.0)	2.69(4)	0.027(7)	-2.2(4)	-	-	-	-	7.2(1.8)	1.52(2)	0.001(1)	-2.2(4)

Table S3. EXAFS fitting results for Pt/Mn-PANI-PPy-PGC using different combinations of scattering paths. N, coordination number, R, the distance between the absorber and scatterer atoms,σ^2,Debye-Waller factor to account for thermal and structural disorders, ΔE_0, inner potential correction. Fitting range, $2.5 \le k(\text{Å}^{-1}) \le 10$ and $1 \le R(\text{Å}) \le 3.2$; Fixed N according to the crystal structure. Error bounds indicated in parenthesis are full errors for N and last digit errors for other parameters

Paths		Pt-Pt				Pt-N				Pt-O				Pt-C			
Fit	χ^2	N	R	σ^2	ΔE_0	N	R	σ^2	ΔE_0	N	R	σ^2	ΔE_0	N	R	σ^2	ΔE_0
1	80.6	6.9(1.8)	2.72(2)	0.012(3)	3.6(5)	1.8(0.2)	2.00(1)	0.001(1)	3.6(5)	-	-	-	-	-	-	-	-
2	93.2	6.3(0.4)	2.71(2)	0.011(3)	3.4(9)	-	-	-	-	1.5(0.2)	3.03(2)	0.001(1)	9.6(3)	-	-	-	-
3	129.7	12.5(0.4)	2.68(3)	0.017(6)	-1.5(3)	-	-	-	-	-	-	-	-	2.3(0.1)	2.01(2)	0.001(1)	-1.5(3)
4	201.7	6.9(0.4)	2.71(3)	0.012(4)	3.6(5)	1.8(0.1)	2.00(3)	0.008(1)	3.6(5)	-	-	-	-	0.0(0.1)	1.93(1)	0.008(1)	3.6(5)
5	170.1	6.9(0.4)	2.71(3)	0.012(5)	3.2(8)	1.8(0.1)	2.00(2)	0.001(1)	3.2(8)	0.3(0.2)	3.18(8)	0.001(1)	3.2(8)	-	-	-	-

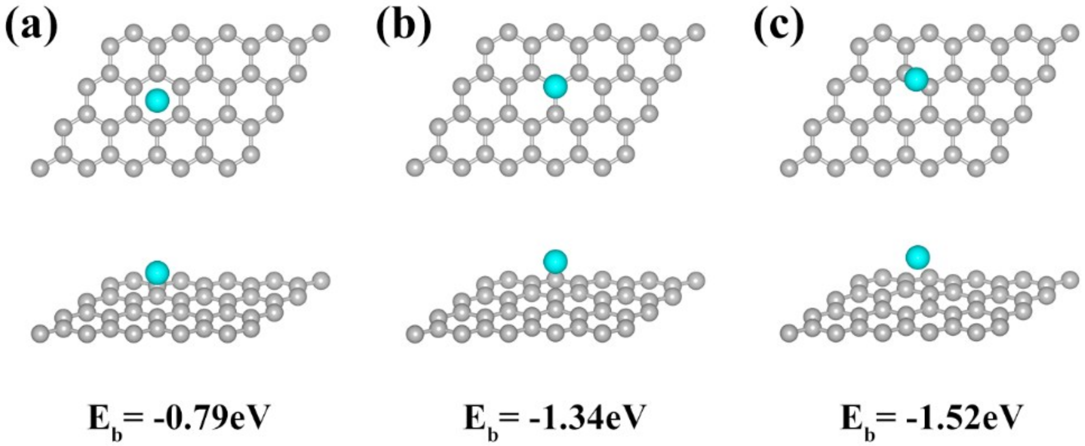

Figure S15. Optimized atomistic structures (top panel: top view; bottom panel: side view) and predicted binding energy of a single Pt atom adsorbed on an un-doped graphene layer on the top of **(a)** the center of a carbon ring, **(b)** a carbon atom, and **(c)** the middle point of two neighboring carbon atoms. In the figure, the gray and cyan balls represent carbon and platinum atoms, respectively.

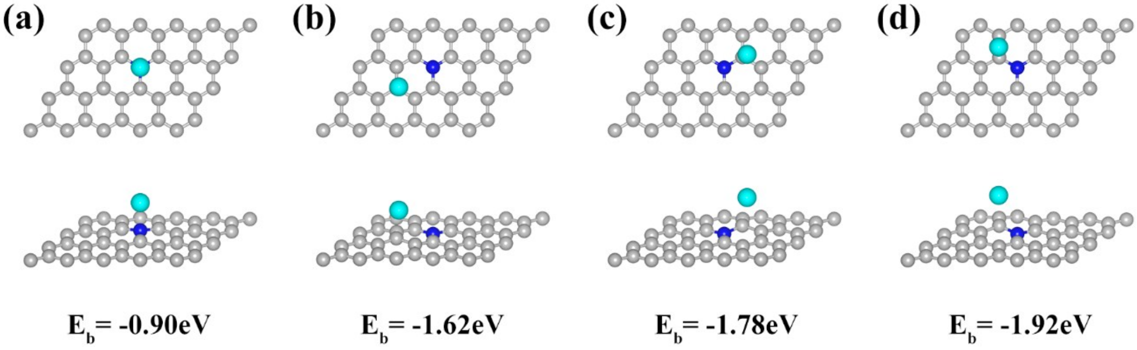

Figure S16. Optimized atomistic structures (top panel: top view; bottom panel: side view) and predicted binding energy of a single Pt atom adsorbed on an N-doped graphene layer on the top of **(a)** the doped graphitic N atom, **(b)** a carbon atom far-away from the doped graphitic N atom, **(c)** a carbon atom adjacent to the doped graphitic N atom, and **(d)** the middle point of two neighboring carbon atoms adjacent to the doped graphitic N atom. In the figure, the gray, cyan, and blue balls represent carbon, platinum, and nitrogen atoms, respectively.

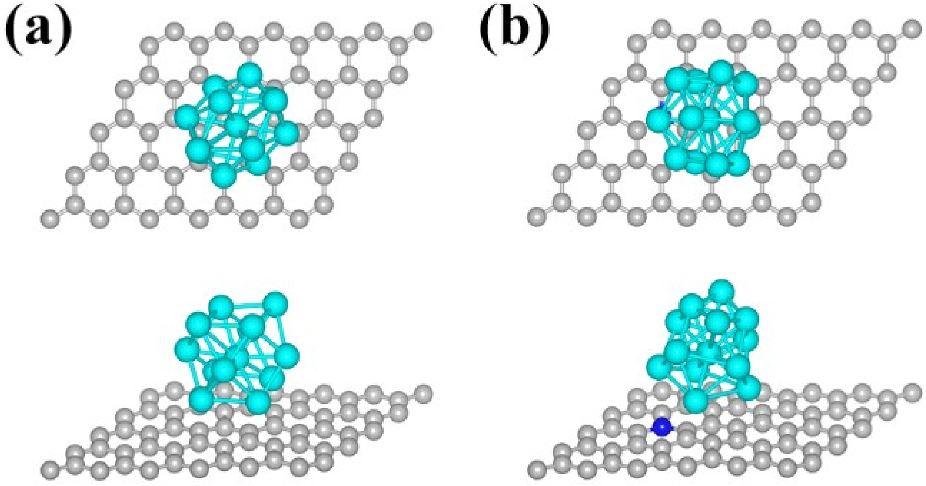

Figure S17. Optimized atomistic structures (top panel: top view; bottom panel: side view) of a thirteen-Pt-atom cluster adsorbed on **(a)** an un-doped graphene layer and **(b)** an N-doped graphene layer. In the figure, the gray, cyan, and blue balls represent carbon, platinum, and nitrogen atoms, respectively.

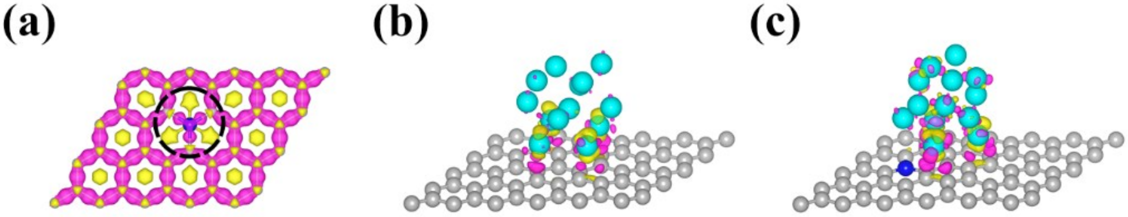

Figure S18. (a) Charge density difference of N-doped graphene layer with respect to the superposition of atomic charge density; Charge density difference of Pt cluster adsorbed **(b)** on an undoped graphene layer and **(c)** on an N-doped graphene layer with respect to the superposition of the charge density of Pt cluster and graphene layer. The magenta and yellow region refers to the increase and decrease in charge density, respectively. The isosurface level is set to be 0.015 e Å^{-3} in **(a)** and 0.007 e Å^{-3} in **(b)** and **(c).** In the figure, the gray, cyan, and blue balls represent carbon, platinum, and nitrogen atoms, respectively.

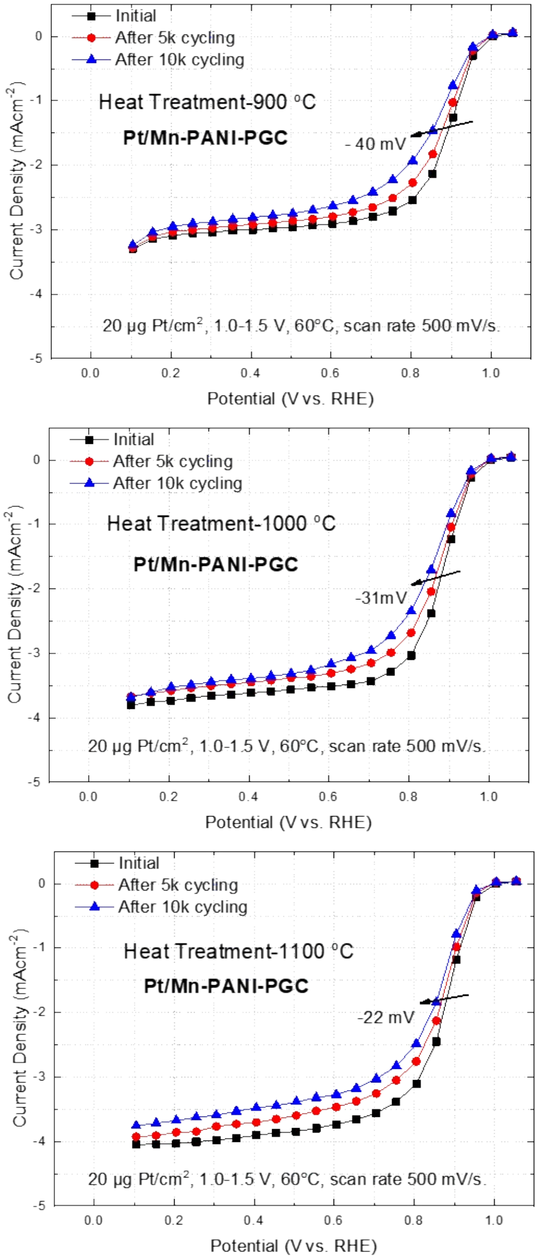

Figure S19. ORR steady-state polarization plots (0.1 M $HClO_4$, 900rpm) during high potential ASTs for Pt catalysts supported by different PGCs derived from various temperature.

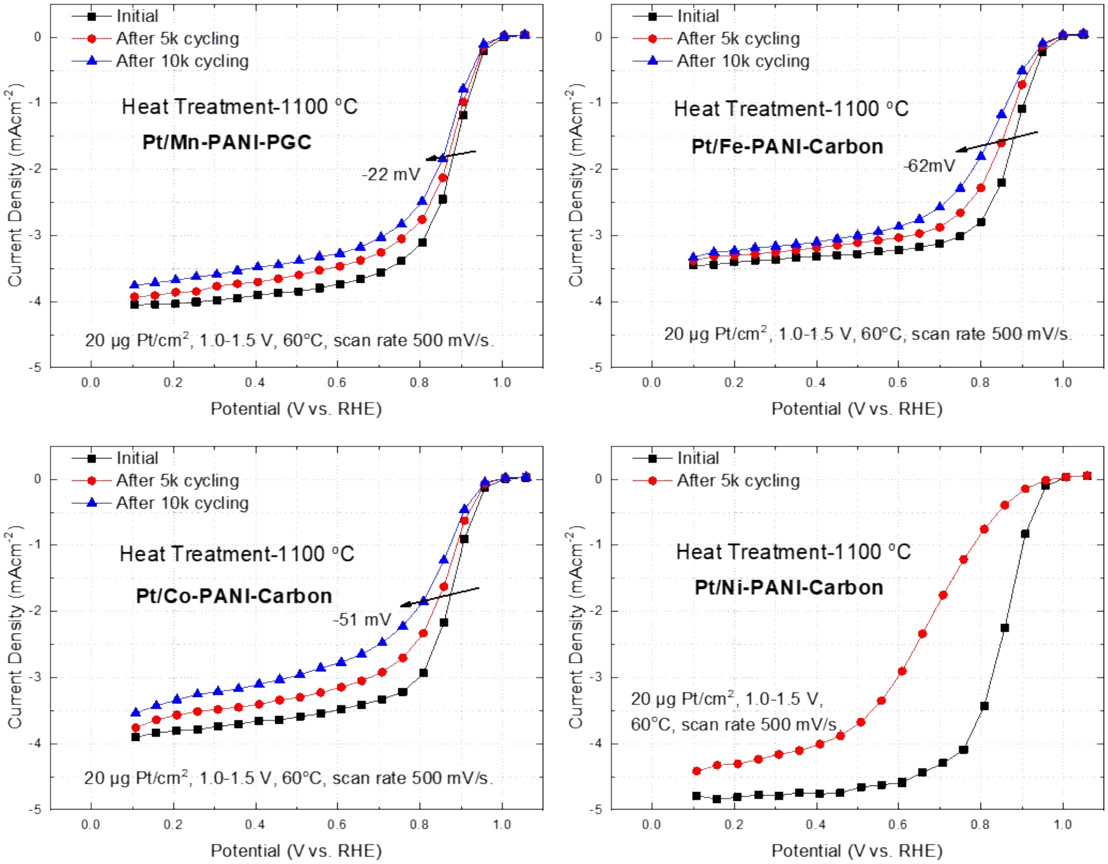

Figure S20. ORR steady-state polarization plots (0.1 M $HClO_4$, 900 rpm) during high potential ASTs for Pt catalysts supported by different hydrogel-based carbon derived from various metals.

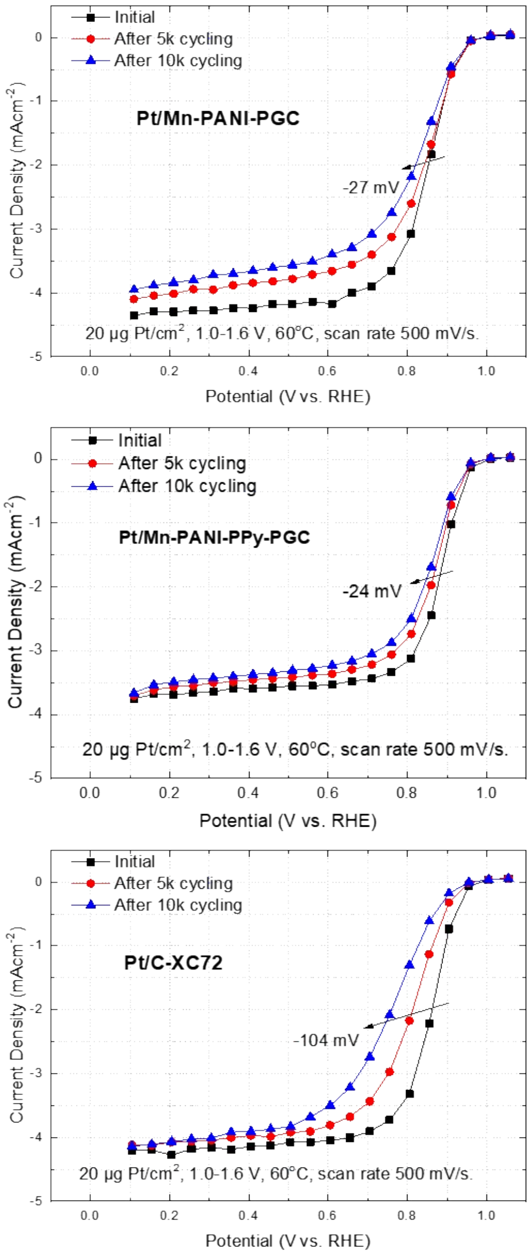

Figure S21. ORR steady-state polarization plots (0.1 M $HClO_4$, 900rpm) during even higher potential ASTs (1.0 – 1.6 V) for different Pt catalysts.

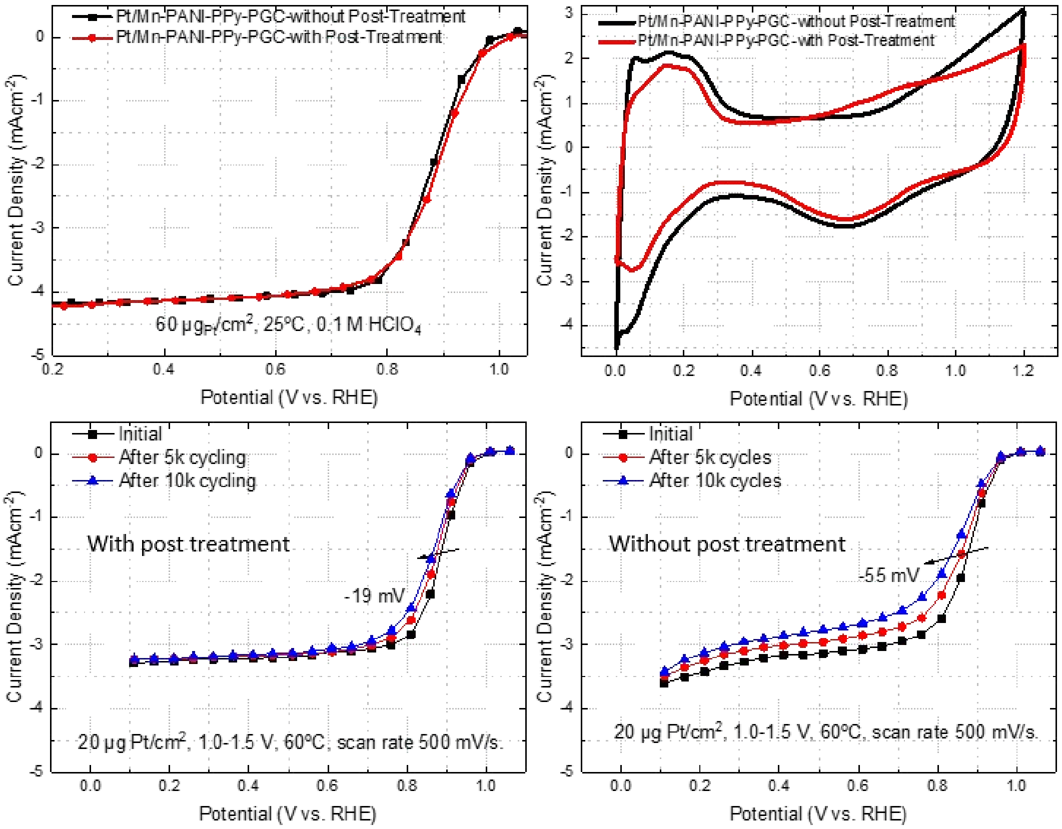

Figure S22. ORR polarization (0.1 M HClO$_4$, 900rpm) and CV plots for Pt/Mn-PANI-PPy-PGC with and without post treatment; and the comparison of their stabilities.

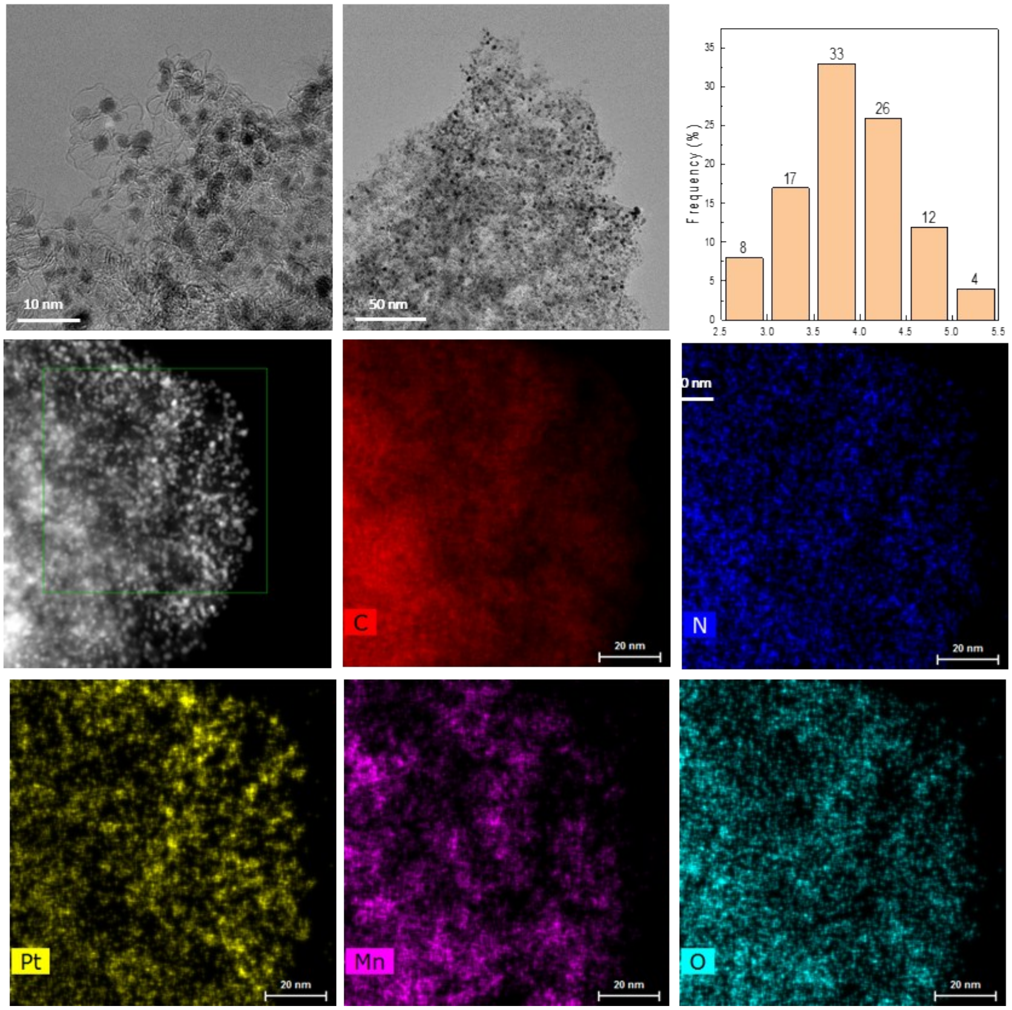

Figure S23. TEM and STEM-EDS images of Pt/Mn-PANI-PPy-PGC without post heat treatment and the corresponding particle size distribution.

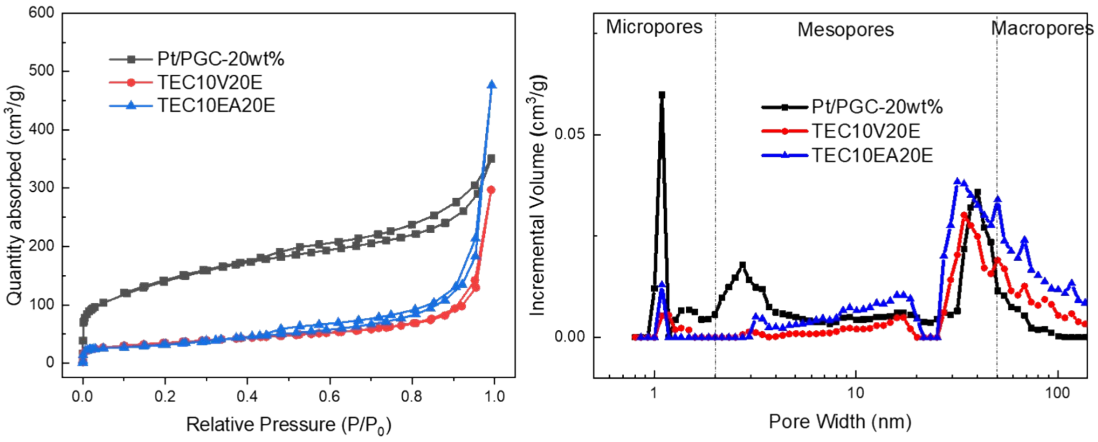

Figure S24. N2 adsorption/desorption plots and corresponding pore size distributions for different Pt/C compared with Pt/PGC.

Table S4. Average particles size of Pt and their ECSA for different Pt/C catalysts.

Pt/C Properties	Pt/PGC	Pt/PGC (Without post treatment)	TEC10V20E	TEC10EA20E	TEC10E20E
Average Pt particles size-nm	5.61	3.83	3.4[6]	3.87[7]	2.94[7]
ECSA-m^2/g (H_{upd} analysis)	67.2	74.6	55.1	38.4	83.7

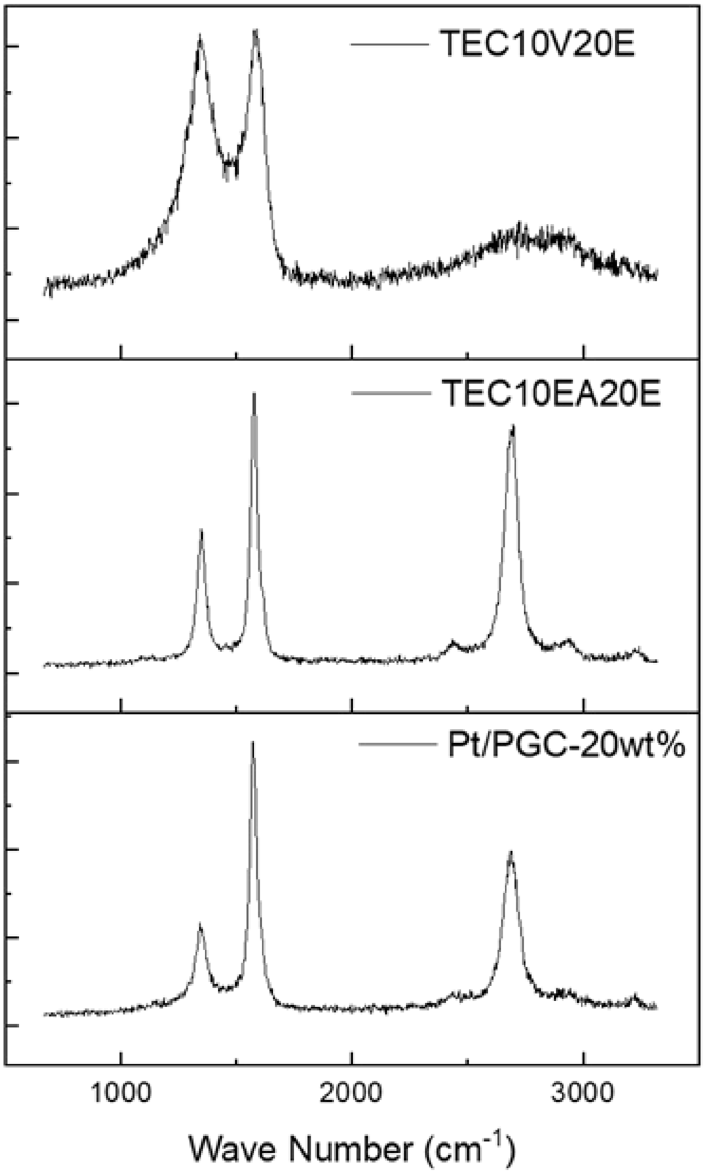

Figure S25. Raman spectra for different Pt/C compared with Pt/PGC.

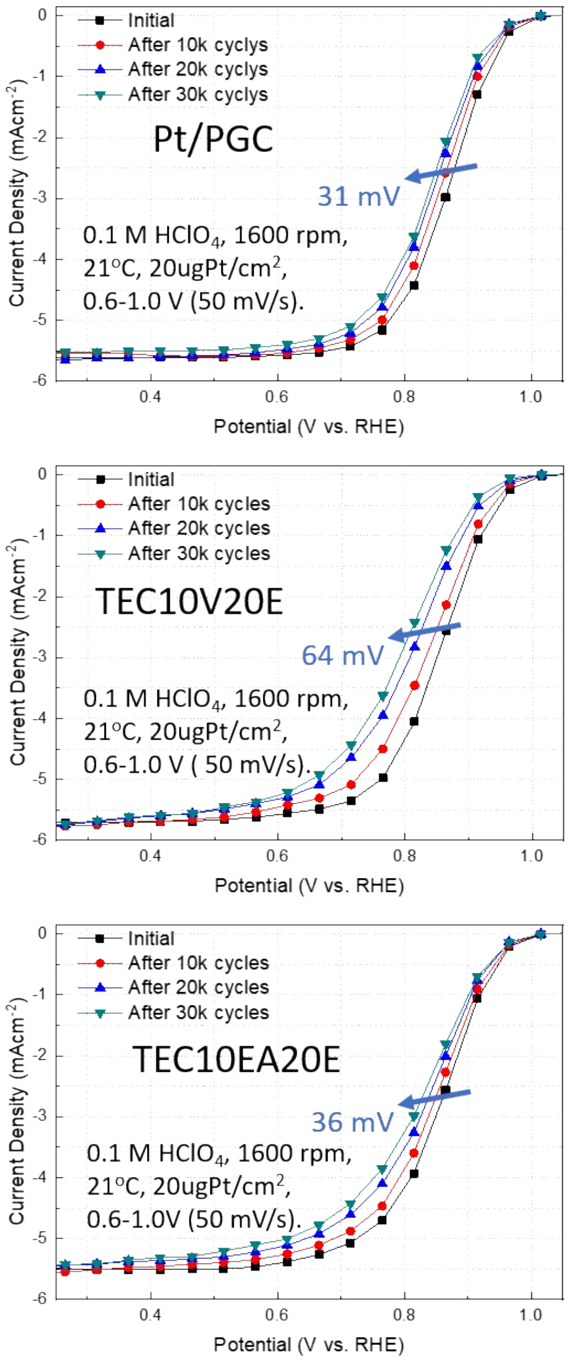

Figure S26. RDE potential cycling stability tests for Pt/Mn-PANI-PPy-PGC, TEC10V20E and TEC10EA20E during low potential range (0.6-1.0V).

(a)

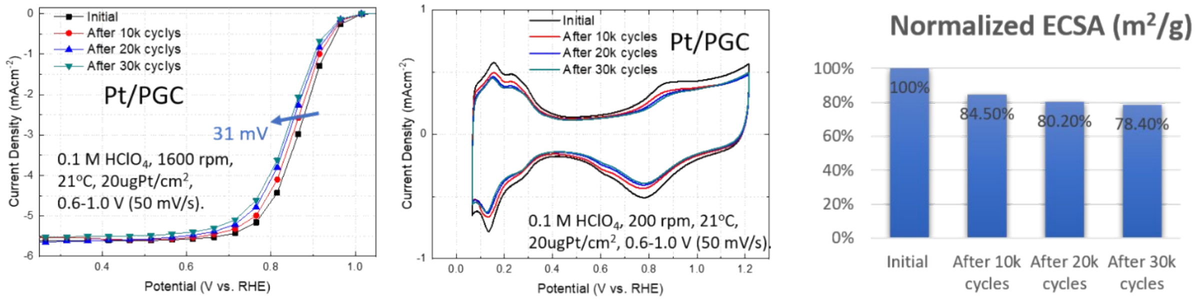
Initial
After 10k cyclys
After 20k cyclys
After 30k cyclys
Pt/PGC
31 mV
0.1 M HClO$_4$, 1600 rpm, 21°C, 20ugPt/cm^2, 0.6-1.0 V (50 mV/s).
Current Density (mAcm^{-2})
Potential (V vs. RHE)
Initial
After 10k cycles
After 20k cycles
After 30k cycles
Pt/PGC
0.1 M HClO$_4$, 200 rpm, 21°C, 20ugPt/cm^2, 0.6-1.0 V (50 mV/s).
Current Density (mAcm^{-2})
Potential (V vs. RHE)
Normalized ECSA (m^2/g)
100%
84.50%
80.20%
78.40%
Initial
After 10k cycles
After 20k cycles
After 30k cycles

(b)

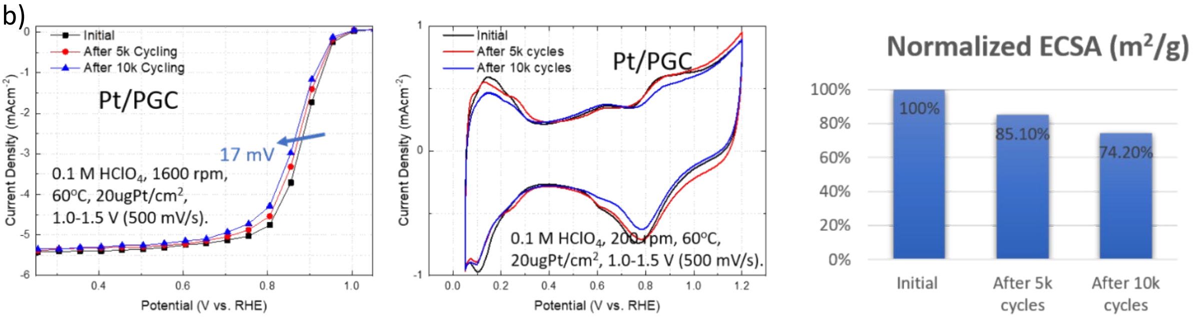
Initial
After 5k Cycling
After 10k Cycling
Pt/PGC
17 mV
0.1 M HClO$_4$, 1600 rpm, 60°C, 20ugPt/cm^2, 1.0-1.5 V (500 mV/s).
Current Density (mAcm^{-2})
Potential (V vs. RHE)
Initial
After 5k cycles
After 10k cycles
Pt/PGC
0.1 M HClO$_4$, 200 rpm, 60°C, 20ugPt/cm^2, 1.0-1.5 V (500 mV/s).
Current Density (mAcm^{-2})
Potential (V vs. RHE)
Normalized ECSA (m^2/g)
100%
85.10%
74.20%
Initial
After 5k cycles
After 10k cycles

(c)

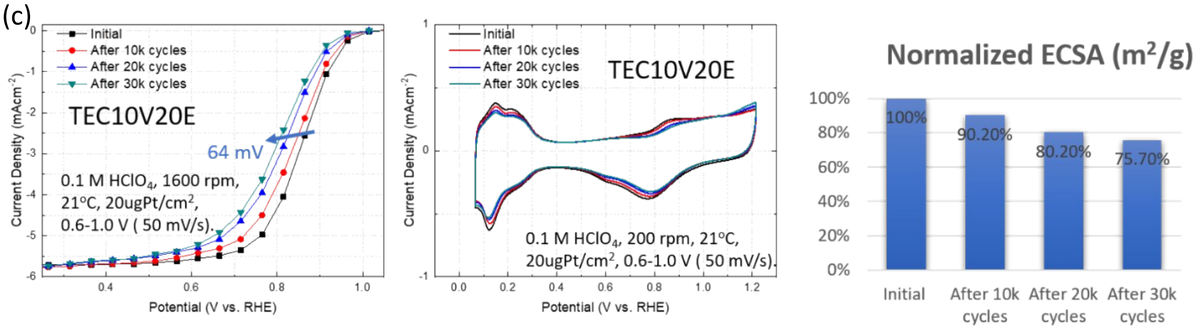
Initial
After 10k cycles
After 20k cycles
After 30k cycles
TEC10V20E
64 mV
0.1 M HClO$_4$, 1600 rpm, 21°C, 20ugPt/cm^2, 0.6-1.0 V (50 mV/s).
Current Density (mAcm^{-2})
Potential (V vs. RHE)
Initial
After 10k cycles
After 20k cycles
After 30k cycles
TEC10V20E
0.1 M HClO$_4$, 200 rpm, 21°C, 20ugPt/cm^2, 0.6-1.0 V (50 mV/s).
Current Density (mAcm^{-2})
Potential (V vs. RHE)
Normalized ECSA (m^2/g)
100%
90.20%
80.20%
75.70%
Initial
After 10k cycles
After 20k cycles
After 30k cycles

(d)

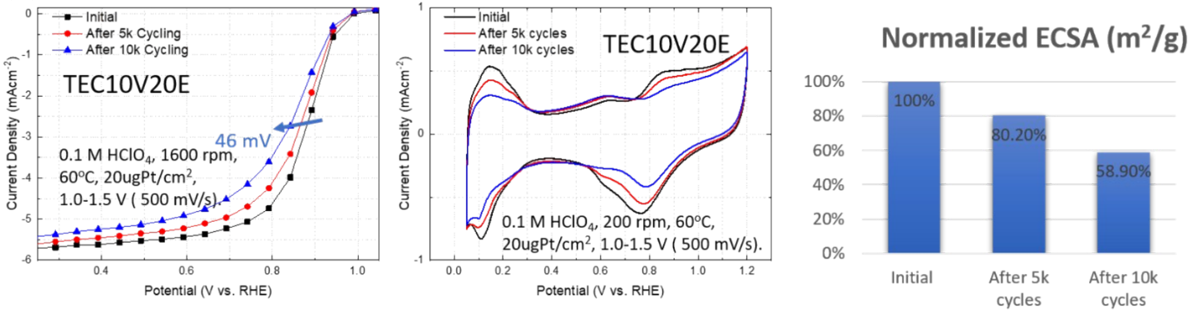
Initial
After 5k Cycling
After 10k Cycling
TEC10V20E
46 mV
0.1 M HClO$_4$, 1600 rpm, 60°C, 20ugPt/cm^2, 1.0-1.5 V (500 mV/s).
Current Density (mAcm^{-2})
Potential (V vs. RHE)
Initial
After 5k cycles
After 10k cycles
TEC10V20E
0.1 M HClO$_4$, 200 rpm, 60°C, 20ugPt/cm^2, 1.0-1.5 V (500 mV/s).
Current Density (mAcm^{-2})
Potential (V vs. RHE)
Normalized ECSA (m^2/g)
100%
80.20%
58.90%
Initial
After 5k cycles
After 10k cycles

(e)

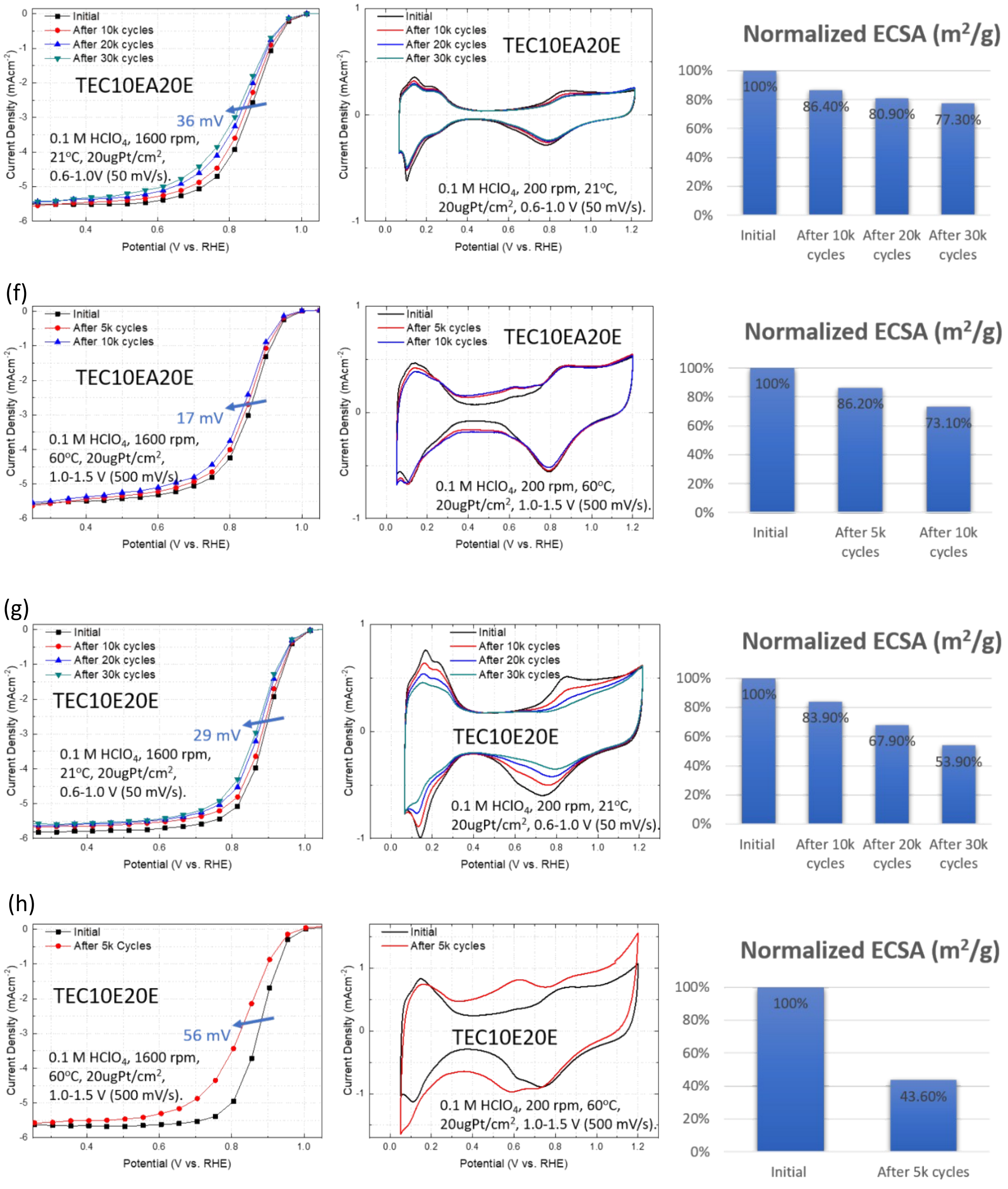

Figure S27. Stability tests results for different Pt/C and Pt/PGC, and their corresponding CV plots and change of ECSA.

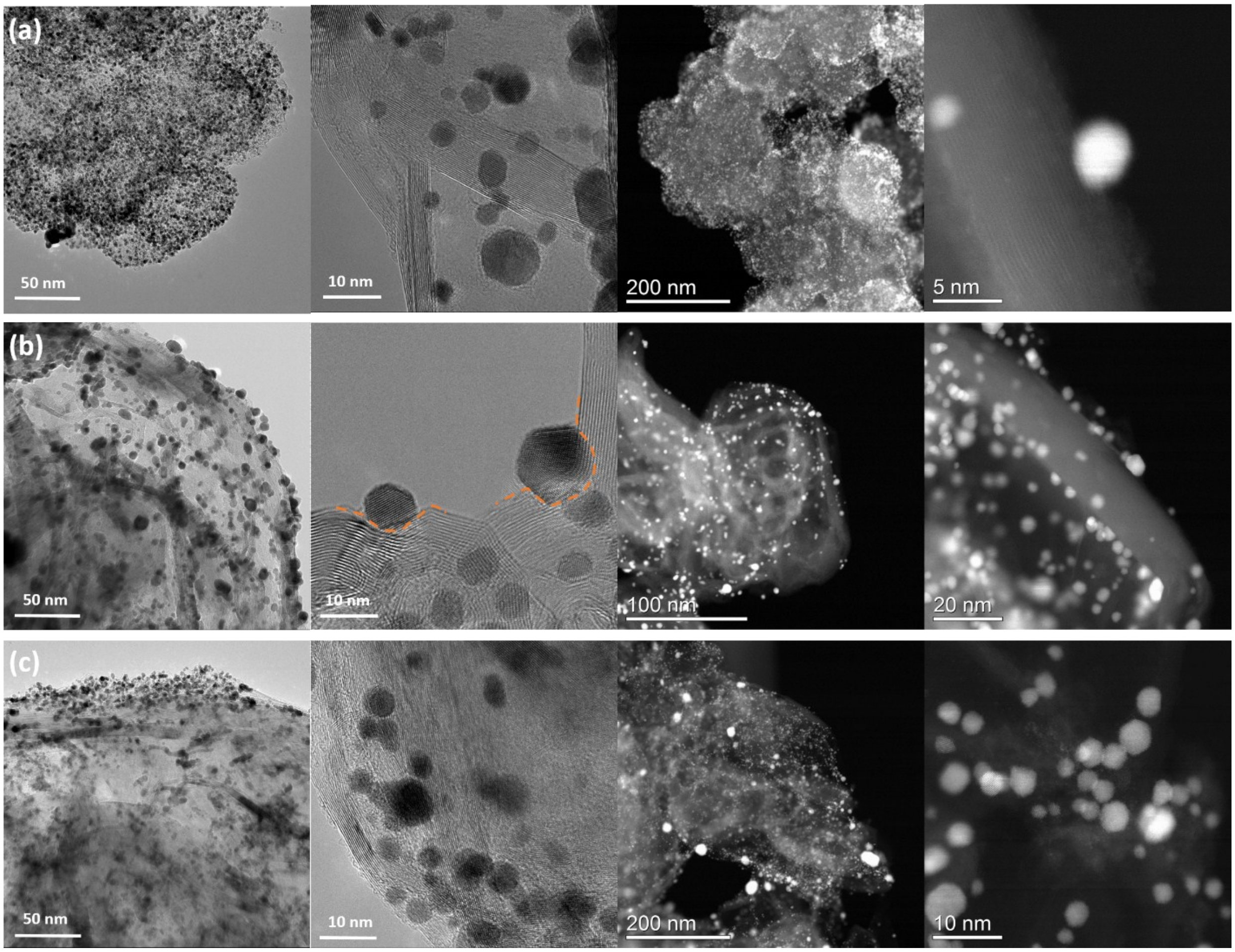

Figure S28. Comparison of the morphology and microstructure among **(a)** original Pt/Mn-PANI-PPy-PGC, and the ones after RDE potential cycling stability tests during **(b)** high potential range and **(c)** low potential range.

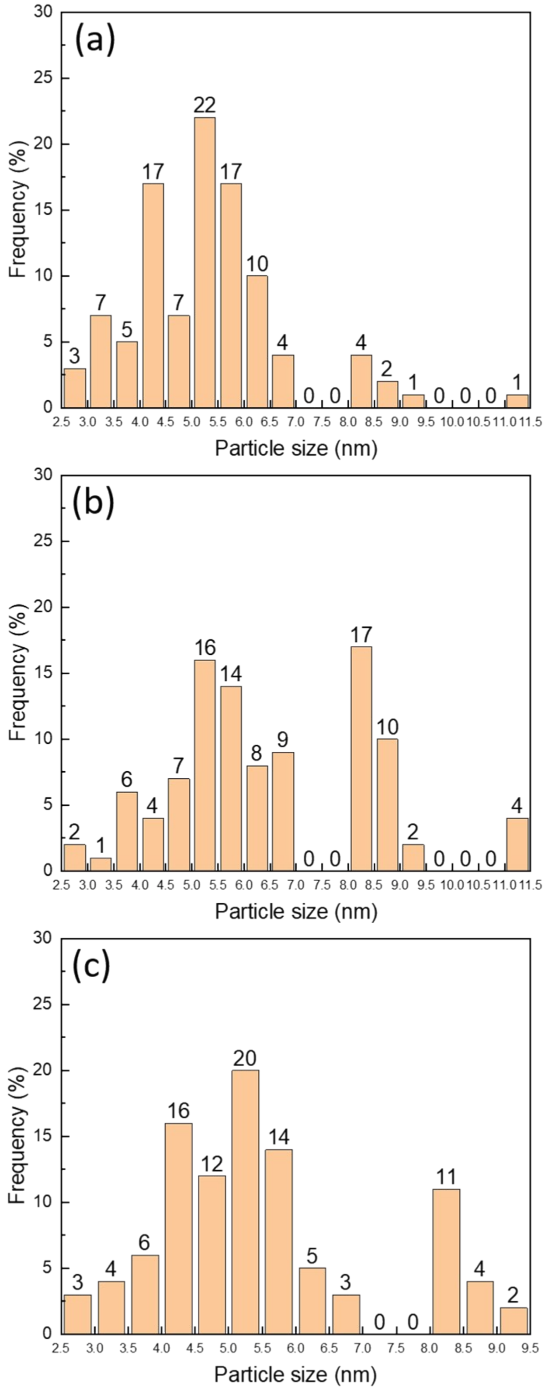

Figure S29. The corresponding Pt particle size distribution of **(a)** Pt/Mn-PANI-PPy-PGC and the ones after **(b)** high potential ASTs and **(c)** low potential ASTs, according to the TEM images in **Figure S28**.

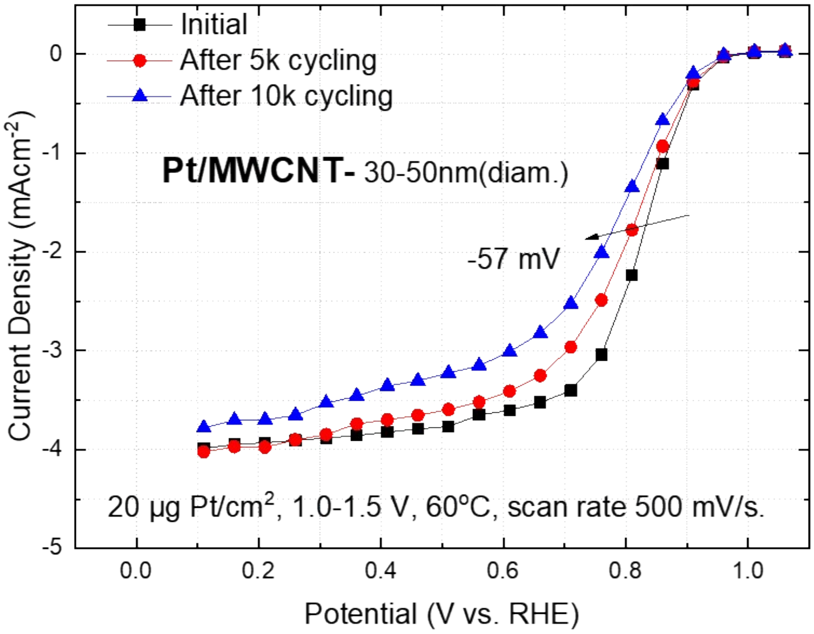

Figure S30. ORR steady-state polarization plots (0.1 M $HClO_4$, 900rpm) during high potential ASTs (1.0 – 1.5 V) for comparative Pt catalyst supported on N-doped MWCNT.

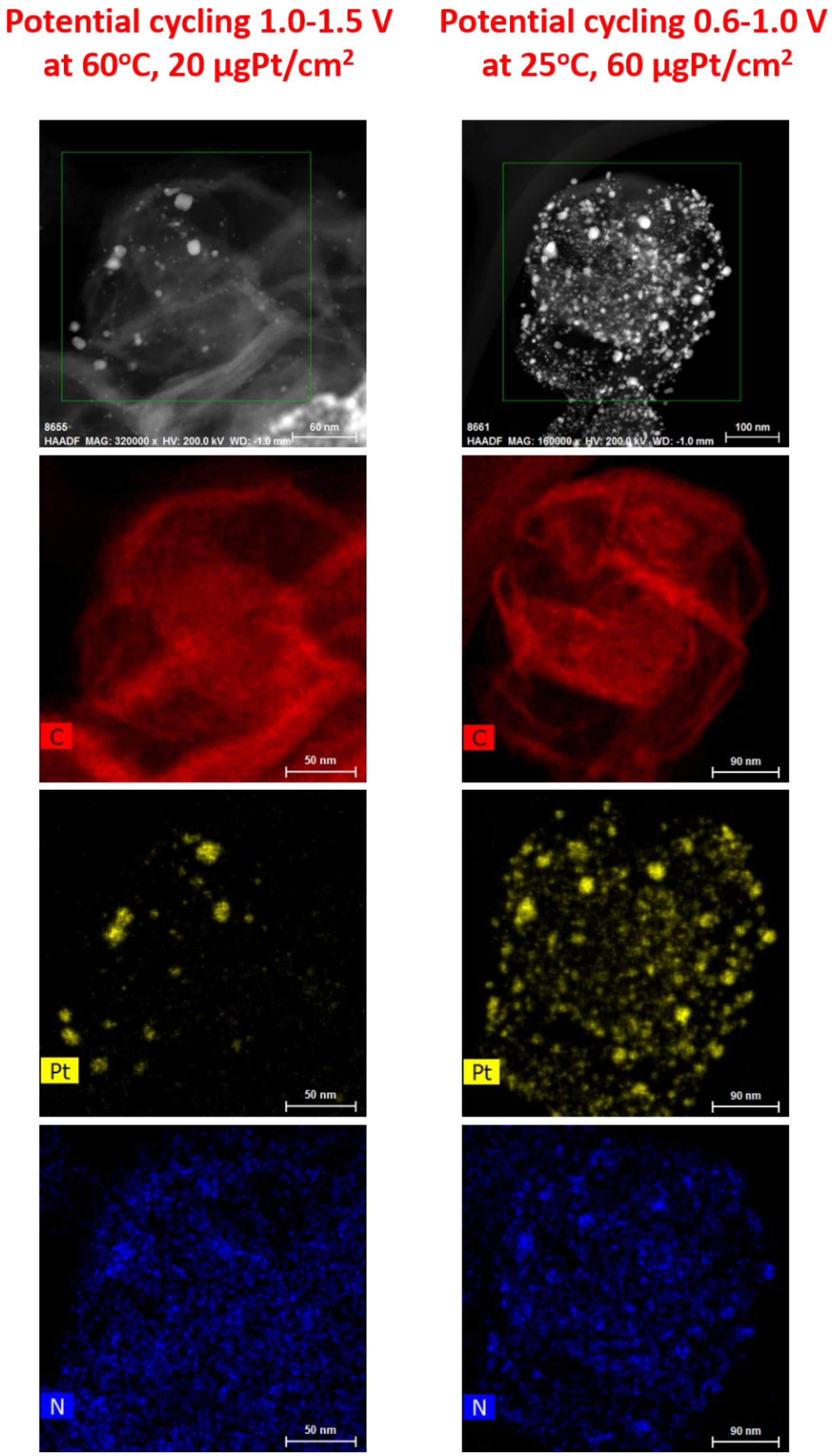

Potential cycling 1.0-1.5 V at 60°C, 20 μgPt/cm²

Potential cycling 0.6-1.0 V at 25°C, 60 μgPt/cm²

Figure S31. Structures and morphologies of Pt/Mn-PANI-PPy-PGC after various ASTs.

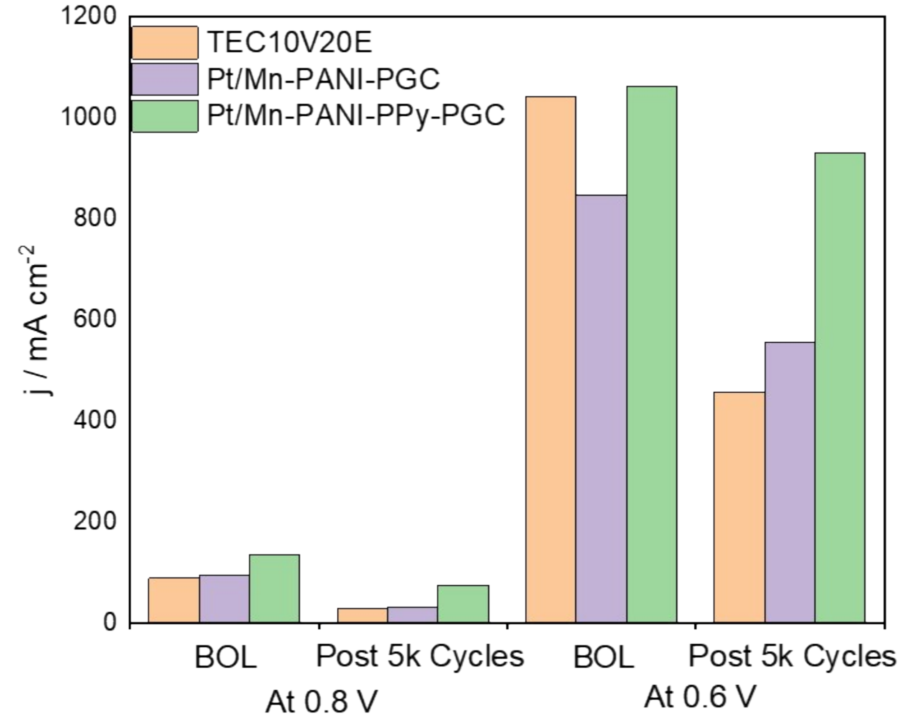

Figure S32. Activity loss summary for fuel cell high potential ASTs at 0.8V and 0.6 V.

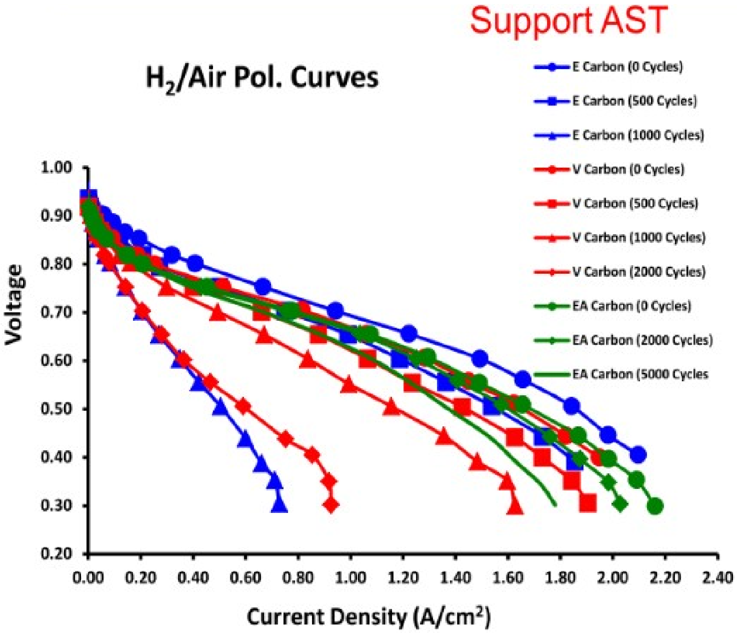

Figure S33. Support stability AST results for different Pt/C catalysts, including E type (high surface area carbon support), V type (Vulcan carbon support), and EA type (Highly graphitized carbon support) supported Pt catalysts from TKK, from 1.0 to 1.5V in MEAs, which is reported by Borup *et al.* in LANL.[8]

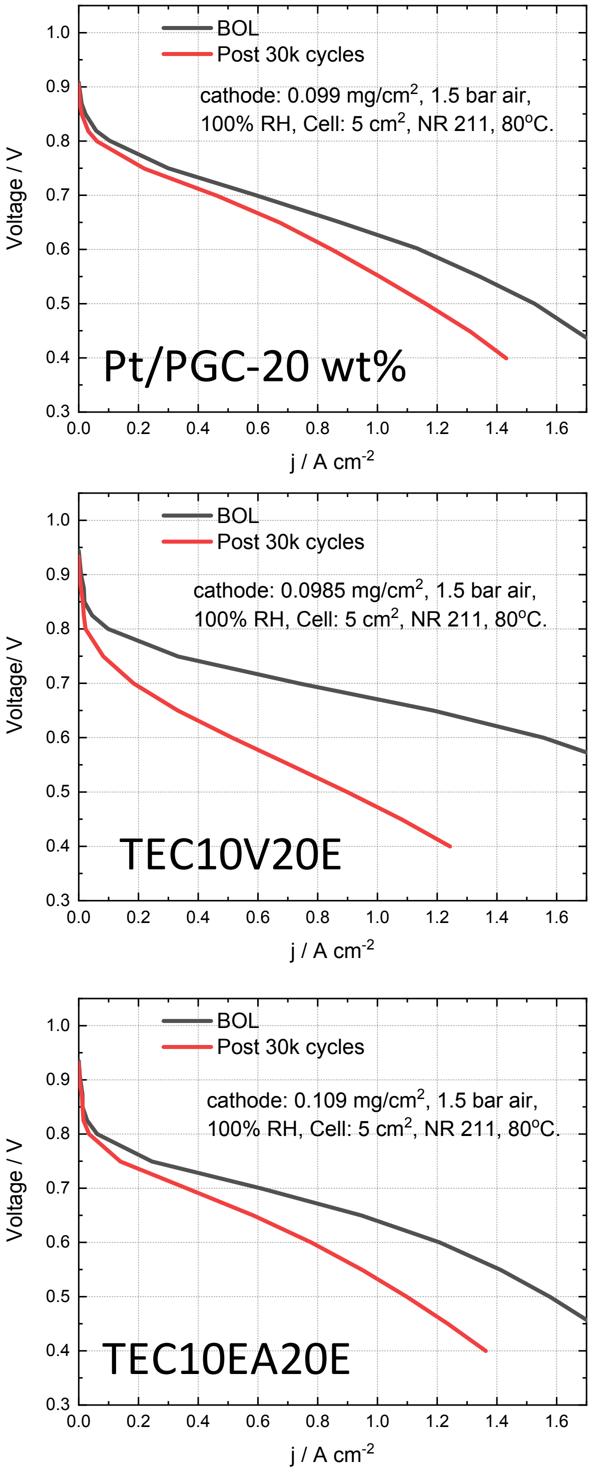

Figure S34. Pt/C catalyst durability ASTs (0.6-0.95 V, for 30, 000 cycles) in MEAs for Pt/PGC developed in this work and other commercially available Pt/C catalysts.

Table S5. A detailed comparison of properties and performance enhancement between the developed PGC and the state of the art XC-72 carbon and other studied carbon supports

Catalysts properties and performance	**$I_{(D)}/I_{(G)}$ in Raman spectra**	**BET surface area (m^2/g)**	**RDE measurements (20ug/cm^2)**						**MEA measurements (0.12mg/cm^2)**					
						Stability-Degradation of $E_{1/2,}$ (V vs. RHE)					Stability- Degradation At 0.8 A/$cm^{2,}$ (mV)			
			$E_{1/2}$ (V vs. RHE)	Mass Activity @0.9V (mA/μg_{Pt}) (IR correction)	Specific Activity @0.9V (mA/cm^2_{Pt}) (IR correction)	Catalyst AST (25°C, 0.6-1.0V, 50mV/s) 30k cycles	Support AST (60°C, 1.0-1.5V, 500mV/s) 10k cycles	EASA (m^2/g)	Mass Activity @0.9V (mA/μg_{Pt})	Mass Activity @0.7V (mA/μg_{Pt})	Catalyst AST (80°C,0.6-0.95V) 30k cycles	Support AST (80°C,1.0-1.5V) 5k cycles	EASA loss after support AST(80°C,1.0-1.5V) 5k cycles (%)	Carbon loss after support AST(80°C,1.0-1.5V) 5k cycles (%)
Pt/PGC	0.32	388	0.878	0.301	0.567	-31	-17	67.2	0.373	4.62	-59	-16	34.4	6.8
TEC10V20E	0.81[9]	153	0.851	0.211	0.383	-64	-46	55.1	0.234	4.07	-150	-200	78.4	29
TEC10EA20E	0.51	113[10]	0.848	0.193	0.482	-36	-17	38.4	--	--	--	-29[11]	--	--
Nitrogen-doped graphene tubes supported Pt[12]	0.71	89	0.887	0.02	0.04	-35	-66	40.1	0.177	2.85	--	52	40.7	11.2
Nitrogen-doped MWCNTs supported Pt	0.34[13]	101	0.876	0.02	0.04	--	-57	43.4	--	--	--	--	--	--

References Reference List

1. Kresse, G. and J. Hafner, *Ab initio molecular-dynamics simulation of the liquid-metal–amorphous-semiconductor transition in germanium.* Physical Review B, 1994. **49**(20): p. 14251.
2. Kresse, G. and J. Furthmüller, *Efficient iterative schemes for ab initio total-energy calculations using a plane-wave basis set.* Physical review B, 1996. **54**(16): p. 11169.
3. Blöchl, P.E., *Projector augmented-wave method.* Physical review B, 1994. **50**(24): p. 17953.
4. Kresse, G. and D. Joubert, *From ultrasoft pseudopotentials to the projector augmented-wave method.* Physical Review B, 1999. **59**(3): p. 1758.
5. Perdew, J.P., K. Burke, and M. Ernzerhof, *Generalized gradient approximation made simple.* Physical review letters, 1996. **77**(18): p. 3865.
6. Mittermeier, T., et al., *Monometallic palladium for oxygen reduction in PEM fuel cells: particle-size effect, reaction mechanism, and voltage cycling stability.* Journal of The Electrochemical Society, 2017. **164**(12): p. F1081-F1089.
7. Mukundan, R., et al., *Accelerated testing of carbon corrosion and membrane degradation in PEM fuel cells.* ECS Transactions, 2013. **50**(2): p. 1003-1010.
8. Borup, R.L., et al., *Durability Improvements through Degradation Mechanism Studies*. 2014, Los Alamos National Lab.(LANL), Los Alamos, NM (United States).
9. Leontyev, I.N., et al., *Characterization of the electrocatalytic activity of carbon-supported platinum-based catalysts by thermal gravimetric analysis.* Mendeleev Communications, 2015. **25**(6): p. 468-469.
10. Macauley, N., et al., *Carbon corrosion in PEM fuel cells and the development of accelerated stress tests.* Journal of The Electrochemical Society, 2018. **165**(6): p. F3148-F3160.
11. Mukundan, R., et al., *Accelerated testing validation.* ECS Transactions, 2011. **41**(1): p. 613-619.
12. Chen, M., et al., *Pt alloy nanoparticles decorated on large-size nitrogen-doped graphene tubes for highly stable oxygen-reduction catalysts.* Nanoscale, 2018. **10**(36): p. 17318-17326.
13. Larrude, D., et al., *Multiwalled carbon nanotubes decorated with cobalt oxide nanoparticles.* Journal of Nanomaterials, 2012. **2012**: p. 53.